



Precision Limits of ultrafast Ultrasound Localization Microscopy

Violinde den Breeijen

Bachelor Thesis
Bachelor of Applied Physics
TU Delft

Delft, June 22, 2020
Supervisors: C. Smith,
B. Heiles,
D. Maresca

The use of ultrafast Ultrasound Localization Microscopy (uULM) is a promising technique for obtaining images with a very high resolution. This technique is based on the localization of sub-wavelength intravascular microbubbles resonating under ultrasound stimulus. Pre-clinical and post-clinical ultrasound applications, such as tumour, microvascular or stroke imaging, are numerous.

This research investigates the theoretical precision limit of uULM in localizing a moving sub-wavelength scatterer. A 1D transducer array and the scatterer are simulated with the Vantage Research Ultrasound Simulator (Verasonics, Kirkland, WA, USA). A large beam is transmitted through the medium by the transducer array and hits the scatterer. As a sub-wavelength scatterer radiates as an omni-directional pressure field, transducer arrays of finite apertures receive a part of this spherical wave back as parabolas (the radio-frequency data, or RF-data), from which a beamformed images (the BF-data) can be reconstructed. The intensity of the RF-data is given in arbitrary units, while the intensity for the BF-data is indicated in decibels. Both the RF-data and BF-data are influenced by different sources of noise, such as jitter and false peaks, which can be modelled with a zero mean white Gaussian noise. In this manuscript, the z -axis is defined to be the direction away from the probe and the x -axis is defined to be colinear to the piezoelectric elements. In Figure 1, an illustration of this process, called Plane Wave Imaging, with the given directions is shown.

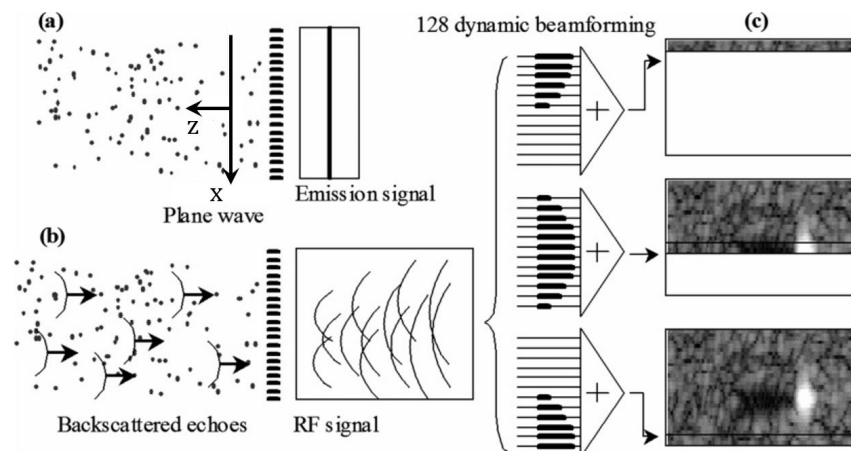


Figure 1: Schematic overview of Plane Wave Imaging: a) plane wave transmission, (b) reception of the backscattered echoes (the RF-signal) and (c) image reconstruction (BF-data). [1]

The localization precision in x - and z -direction are computed for different intensities, different signal-to-noise ratios (SNR's) and different depths z for both the RF-data and the BF-data. For the RF-data, there is a clear relation between the depth of the scatterer and the localization pre-

cision: if the scatterer is moving further away, the minimum standard deviation decreases due to attenuation in tissues. For example, for a depth of 11 mm and a SNR of 29 dB, one is able to localize the microbubble with a precision of 10 nm in x -direction and 50 nm in z -direction based on the RF-data, while this decreases to respectively 1 μm and 0.5 mm for a depth of 21 mm.

The BF-based precision limits are less dependent on depth: for different depths, the limits remains approximately the same, being 0.5 μm in x -direction and 1 μm in z -direction for an intensity of 20 dB and a SNR of 29 dB. A remarkable result is that the localization using the radiofrequency data is more precise compared to the beamformed images if the scatterer is close to the transducer array. However, after a certain depth, the BF-based localization surpasses the RF-based one. This difference in precision is due to the beamforming process: to translate radiofrequency data in a readable image, one need to sum the energy scattered back and select that value as the pixel intensity for the final image. This process, called beamforming, can be done on the fly or in post-process. In this research, it is complex to compare the initial values, being the SNR, the maximum intensity value and the dependence on depth, between the RF- and BF-data.

The localization precision for the RF-data and for the BF-data reacted similar to changes in the amount of noise. For a high SNR, the position of the scatterer can be determined more precisely compared to a situation with a low SNR. For example, the RF-data revealed a localization precision of 1 nm in x -direction for a SNR of 33 dB, while a SNR of 23 dB resulted in a precision of 10 mm for the same intensity and depth.

	Page
1 Introduction	1
2 Theory	3
2.1 Abbe's Resolution Limit	3
2.2 Optical Imaging Method - FPALM	4
2.2.1 Introduction to FPALM	4
2.2.2 Resolution limits for FPALM	4
2.3 Acoustic Imaging Method - uULM	5
2.3.1 Analogy between FPALM and uULM	5
2.3.2 Plane Wave Imaging	6
2.4 The Maximum Likelihood Estimation	7
2.4.1 The goal of MLE	8
2.4.2 The Maximum Likelihood Estimate	8
2.5 The Cramér-Rao Lower Bound	9
2.5.1 Fisher Information	9
2.5.2 The Fisher Information in case of k parameters	10
2.5.3 The Efficiency of an Unbiased Estimator	10
2.6 Localization Precision Limits in uULM	10
2.6.1 Computing the Cramér-Rao Lower Bound	11
2.6.2 Specifications for the BF-data	13
2.6.3 Specifications for the RF-data	14
2.6.4 Resulting super-resolution	14
2.7 Sources of Noise	14
2.7.1 Sampled Data	14
2.7.2 False Peaks and Jitter	15
2.7.3 Readout noise	15
2.7.4 Movements	15
3 Method	16
I. Collect data	16
II. Approximate the PSF	17
III. Derive the Fisher Information Matrix	19
IV. Collect more data points	19
4 Results & Discussion	21
4.1 Localization Precision Limits	21
4.1.1 Beamformed Images	21
4.1.2 Radiofrequency Data	23

4.2	Interpretation	24
4.2.1	Variation in Depth	24
4.2.2	The Influence of Noise	26
4.3	Resulting super-resolution	26
4.4	Further Recommendations	27
4.4.1	Approximations	27
4.4.2	Increasing the range of measurements	28
4.4.3	The Grid	29
4.4.4	Position of the Scatterer	29
5	Conclusion	31
	Bibliography	33
6	Supplementary Data	37
A	Appendix	39
A.1	Optical beamforming	39
A.2	Ultrasound Beam Forming	40
A.3	Find the point spread function	40
A.3.1	Determine the sound pressure	40
A.3.2	Find the ultrasound pulse-echo	42
A.3.3	Simplifications	43
A.4	Localization Precision in RF-data with noise fluctuations	44
B	Matlab Scripts	46
B.1	RF-data	46
B.2	BF-data	52

Introduction

Resolution is a measure of the ability of a microscope to see things in detail. The achievable resolution of a conventional microscope is limited by the diffraction barrier, the so called Abbe's Limit. Traditionally, this barrier resulted in an optical resolution of about $0.2 \mu\text{m}$. [2] In ultrasound imaging, the resolution limit depends on the wavelength and it is inversely proportional to the penetration depth. To image small animals, the resolution usually equals around $100 \mu\text{m}$ for a penetration depth of 2 cm. For human, the resolution is higher with higher penetration depth. In the past few years, the use of super-resolution microscopy in the medical world has been successfully growing. One is now able to create super-resolution images. For example, tissues and blood vessels can be imaged very precisely, from which vascular damages can be detected. Besides, pre-clinical and post-clinical ultrasound applications, such as tumour, microvascular or stroke imaging, are numerous

An example of a procedure to create super-resolution images is the fluorescence photo-activated localization microscopy (FPALM). This is an optical technique that uses the stochastic blinking of fluorescent molecules to visualize vascular systems. Currently, a resolution up to 10 nm can be achieved with this method, which is small compared to cells ($1 \mu\text{m}$ to $100 \mu\text{m}$), but large compared to complex molecules (1 nm). [3] However, the problem of optical microscopy is due to the imaging depth in opaque biological tissues rather than the resolution.

To reach new depths in biological tissues, one can use acoustic waves for imaging. Echography is a whole field of radiology, using ultrasound for vascular, bone and soft tissue imaging. Ultrasound techniques make use of a small probe (a transducer) and a gel, placed directly on the skin. High-frequency sound waves are transmitted through the gel into the body. [4] The back-bounced waves are collected by the probe. With these sounds, an image can be created by a computer.

In this research, the possibilities of ultrafast Ultrasound Localization Microscopy (uULM) to track microbubbles administered in blood vessels are evaluated. These microbubbles are gas-filled vesicles, with lipid or protein outer shells. When hit by an ultrasound wave, the microbubbles scatter a part of the wave back and start to vibrate, producing high energy echoes. These echoes are clearly visible in echography. Thanks to these bright echoes, it has been shown than one can use the microbubbles much like the fluorescent molecules in FPALM to break the diffraction limit. [5]

The aim of this research is to find the precision with which uULM can pinpoint the position of a single sub-wavelength scatterer. Knowing this precision, will provide information about the resolution of the used method. If the localization precision limits are very small, the position of the microbubble can be determined very precisely, providing more information about, for example, the

vascular system compared to high precision limits. The localization precision limits are given by the Cramér-Rao Lower Bound, the minimum variance for a certain parameter. In Chapter 2, the theory about this research will be provided. The used method are elaborated upon in Chapter 3. This is followed by a presentation and a thorough discussion of the results in Chapter 4. Besides, some recommendations for further research and improvements are given. Lastly, a conclusion of this research will be presented in Chapter 5.

This research is part of the Bachelor Applied Physics at Delft University of Technology.

Theory

In this chapter, the relevant theory for this research is described, starting with the introduction of Abbe's Limit, followed by an overview of fluorescence photo-activated localization microscopy (FPALM). After this, the process of uULM (ultrafast Ultrasound Localization Microscopy) will be evaluated and two statistical concepts, being the Maximum Likelihood Estimation and the Cramér-Rao Lower Bound, will be introduced. This chapter will conclude with the theoretical localization precision limits using uULM and an overview of different sources of noise.

2.1 Abbe's Resolution Limit

Both the optical and the acoustic imaging techniques are limited in resolution. In this section, the classical diffraction limit will be discussed.

If light passes an object, light waves will bend into different directions, called diffraction. The way of bending is described by the Huygens-Fresnel principle. [6] This diffraction also occurs when light passes an aperture, restricting the highest possible resolution for microscopical instruments. This limit on the achievable resolution is called the diffraction barrier, or Abbe's Limit, as given in the following equation:

$$d = \frac{\lambda}{2\text{NA}} \quad (2.1)$$

in which d represents the resolvable distance, λ the wavelength of light and NA the numerical aperture. [6] This numerical aperture is equal to $n \sin \theta$, in which n represents the refractive index in a medium and 2θ equals the maximal angle of the cone of light that can exit or enter the lens, as shown in Figure 2.1. [7]

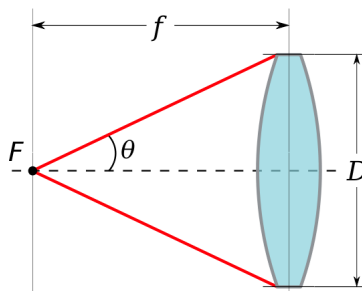


Figure 2.1: Numerical aperture of a lens. [7] f represents the focal length and F the focal distance. The diameter of the lens is given by D . θ equals half of the maximal angle of the cone of light that can enter or exit the lens

Due to Abbe's Limit, an optical instrument is not able to distinguish two different objects if the distance between them is less than the resolvable distance d , as introduced in equation (2.1). [8]

Abbe's limit holds for sub-wavelength sources. One single image of two sub-wavelength sources will produce a diffraction limited image. To produce super-resolution images, the sub-wavelength sources have to be localized with a higher precision. One method to achieve these super-resolution images is using fluorescence photo-activated localization microscopy (FPALM). Instead of forming a single image, FPALM will activate one of the sources. After localizing it with sub-wavelength precision, another source is activated and localized. A final image is then formed by adding the two sub-wavelength positions in a super-resolved image. In other words, FPALM overcomes the Abbe's limit by the decorrelation of space and time. In the next section, an overview of this process is given.

2.2 Optical Imaging Method - FPALM

In this research, the precision with which uULM can pinpoint the position of a single sub-wavelength scatterer is studied. Before explaining the process of uULM, it is useful to look into other imaging techniques, such as optical microscopy. uULM mimics FPALM, by taking benefit of ultrafast ultrasound imaging of transient changes in highly concentrated solution of ultrasound contrast agents. [9] In this section, the FPALM method, as well as its resolution limits, will be evaluated.

2.2.1 Introduction to FPALM

FPALM is an optical imaging technique that uses fluorescent molecules to achieve super-resolution images. These images are created by using stochastic blinking of switchable fluorescent labels. [5] Dye molecules with a radius of approximately 2 nm [10], located at the surface of a certain subject, are excited with lasers. The activation illumination intensity determines the activation rate. First, a high frequency (approximately 400 nm) is used to excite non-fluorescent molecules. After this, a lower frequency can be used to excite these molecules again. [10] In this way, a portion of the molecules begin to fluoresce. An image can be created by capturing the light coming off, being a dark picture with some bright stars. [11] Since there are only a very few molecules visible at a given time, their location can be determined very precisely. By repeating this process over a thousands of times and combining the obtained images, one is able to create a super-resolved image. [5]

2.2.2 Resolution limits for FPALM

With this use of fluorescent molecules, FPALM is able to go beyond the diffraction limit. [12] It is however important to stop the fluorescing of the molecules after making each picture. Otherwise, the accumulation of active molecules will bring back the diffraction limit and the resolution will be limited again. Therefore, photobleaching is used to inactivate the fluorescing molecules. [10] After a certain number of excitation cycles, depending on the type of molecule, a fluorescent molecule transforms its single state into a triplet state. This causes irreversible modifications in the covalent bonds of the fluorophores, resulting in a molecule unable to fluoresce. This process is called photobleaching. [13]

The resulting super-resolution is influenced by the localization precision and the particle density. [14] The maximal achievable resolution is determined by the sampling density, the instrument

resolution and the SNR. [15]

The standard deviation of the localization in FPALM σ_{FPALM} can be determined using the following equation: [3]

$$\sigma_{\text{FPALM}} = \sqrt{\left(\frac{\sigma_{\text{PSF}}^2 + \frac{a^2}{12}}{N}\right) \cdot \left(\frac{16}{9} + \frac{8\pi\sigma_{\text{PSF}}^2\theta_{bg}^2}{a^2N^2}\right)} \quad (2.2)$$

in which N represents the number of collected photons, a the pixel size of the imaging detector, θ_{bg} the average background signal and σ_{PSF} the standard deviation of the point spread function. [3]

Using FPALM, one is able to create images with a resolution up to 10 nm. [3] This is a huge improvement compared to the classical resolution of 0.2 μm due to Abbe's Limit as stated in 2.1. With this resolution of 10 nm, cells (with a size from 1 μm to 100 μm) can be images properly. However, to image complex molecules (with a size around 1 nm), a higher resolution is needed. [3] More about FPALM can be found in the Appendix part A.1. In this section, an overview of the imaging process is given.

Transforming FPALM into an acoustic version, results in ultrafast Ultrasound Localization Microscopy (uULM). In the next section, an overview of this technique will be given.

2.3 Acoustic Imaging Method - uULM

Ultrafast imaging is a new technique in ultrasound. Instead of sending focused acoustic beams and reconstructing an image line by line, unfocused plane waves are sent through a material. Implementations relying on plane-wave transmission can reach hundreds to thousand of frames per seconds. [9] In this research, the precision with which uULM can pinpoint the position of a single sub-wavelength scatterer is studied. By determining the positions and flows of microbubbles with uULM, one is able to make a construction of whole vascular systems. [16]

2.3.1 Analogy between FPALM and uULM

Both FPALM and uULM are localization methods that make use of Rayleigh particles. If a Rayleigh particle is hit by a plane wave, it starts to reflect spherical waves. In FPALM, sub-wavelength emitters reflect optical waves in all directions. uULM makes use of reflectors to reflect sound waves omni-directional. Besides, uULM mimics FPALM by taking benefit of ultrafast ultrasound imaging of transient changes in highly concentrated solution of ultrasound contrast agents. [9]

Apart from the analogous between FPALM and uULM, there are also some differences between the optical and the acoustic method. To start with the position of the scatterer: in FPALM, one can choose where the static emitter are located, while this is not the case for the moving reflectors in uULM. Because of these characteristics, uULM lends itself to the imaging of whole vascular networks, while this is not possible with using FPALM. Also the resolution characteristics of both methods vary: in FPALM, the resolution only depends on the number of produced images, while for uULM, the resolution is also influenced by the flow and the vascular shapes in the system.

2.3.2 Plane Wave Imaging

The imaging process of uULM is called plane wave imaging, which aims to minimize the number of transmissions needed to form an image, maximizing the frame rate. [17] Due to this high frame rate, the process is sometimes called ultrafast. Ideally, one wants to have just one transmission event per image. In this case, the frame rate is only limited by the speed of sound in its medium, by the time needed to form an image and by the desired imaging depths. [17] In essence, this method achieves a homogeneous and very wide beam (as wide as the aperture) by approximating the generation of a plane wave in transmission. [17] This is done by exciting all the transducer elements with the same phase at each event, followed by processing these signals with different phase sets and amplitudes in the receive phase. In this way, multiple lines are generated in parallel. The final image is then formed by combining all the lines that are received from an echo signal with just one single transmission event. [1]

In plane wave imaging, the temporal resolution is maximized, to the cost of all other image features: the signal-to-noise ratio (SNR) is low and the penetration depths are small due to a very low pressure amplitudes. Besides, the obtained image has a low quality in spatial resolution and only a small contrast. [17] With image compounding, one can increase the contrast of uULM. By combining images made with plane waves propagating under different angles with the transducer array, to the cost of the very high frame rate, one can improve resolution and contrast. [18]

Without compounding, very high frame rates can be achieved, making this method suitable to image fast phenomena, where temporal resolution is much more important than spatial resolution. [18]

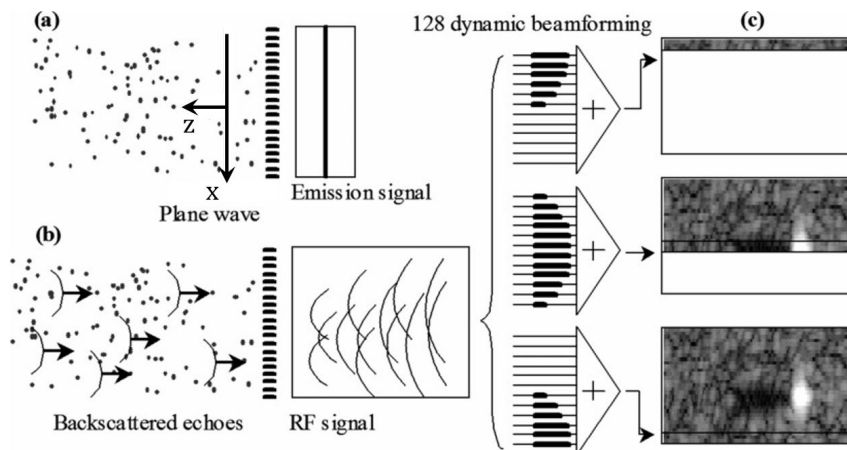


Figure 2.2: Schematic overview of plane wave imaging: (a) plane wave transmission, (b) reception of the backscattered echoes and (c) image reconstruction. [1]

In essence, plane wave imaging consists of three steps, shown in Figure 2.2.

- a) **Plane Wave Transmission.** A large beam with unique pulsed plane wave is transmitted through the medium. In this way, the medium is insonified by the ultrasonic array. [1]
- b) **Reception of the backscattered echoes.** Due to heterogeneities of the medium, the wave

scatters back and hits the array. This echo signal is denoted as the RF-signal (radiofrequency signal). Inhomogeneities result in depth and field of view (FOV) variations in the model. This, however, is out of scope for this research and can be estimated from the data at a later stage. During this project, the medium is considered to be homogeneous, thus assuming uniform properties over its whole volume. Therefore, all backscattered echoes are due to collisions with the sub-wavelength microbubble. The radiofrequency data is measured as an electric signal and is proportional to acoustic pressure. In essence, the RF-data represents what is felt by the transducer over time. Applying a voltage to the material, results in a vibration of the transducer array, consisting of piezoelectric crystals. These vibrations produce an ultrasonic burst of a few cycles. By using different delays, a whole volume can be scanned. When the transmitted signal hits a certain object, a reflected field will go back to the transducer array. When recording the echo, the received signal is a pressure hyperboloid, with its center and shape depending on the position of the source, as can be seen in step b) from Figure 2.2.

The position of the source can then be found by using the reception time τ_i , being the sum of the time for the plane wave to propagate from the transducer i (positioned at (x_i, y_i, z_i)) to the source (positioned at (x_0, y_0, z_0)) and the time for the echo to propagate back from the source to the transducer. This sum is expressed in the time-of-flight equation: [9]

$$\tau_i = \frac{z_0}{c} + \frac{\sqrt{(x_i - x_0)^2 + (y_i - y_0)^2 + (z_i - z_0)^2}}{c} \quad (2.3)$$

- c) **Image reconstruction.** In the last step, an image is reconstructed from the RF-data with the use of delay and sum beam forming. Adding different amounts of delay to the transducer signals by changing the angle of incident and summing them, will result into an acoustic antenna with a main lobe and suppressed side lobes. [19] All different angles represent different parts of the surface. To reduce the error from the side lobes, uniformly distributed arrays are used. Since the transmitted beam has no focusing, the echoes coming from the same scatter are added coherently during the reception mode. This parallel processing determines the image resolution. [1] The RF-data provides a hyperboloid for each pixel. Summing the acoustic pressure along a certain hyperboloid, results in one value used for that pixel in the final image. The intensity of the beamformed images (BF-data) is converted into decibels, indicating the difference between the noise and the maximum backscattered echo.

Another schematic overview of plane wave imaging can be found in Figure 2.3. More about array beam forming can be found in the Appendix part A.2. Here, the difference between Linear Array Beam Forming and Phase Array Beam Forming will be evaluated.

In the next section, an overview about the estimation of a Maximum Likelihood Estimator and the Cramér-Rao Lower Bound, being its minimum variance, will be given. After this, the resulting localization precision limits for both the radiofrequency data and the beamformed images will be discussed.

2.4 The Maximum Likelihood Estimation

The aim of this research is to determine the localization precision limits for a moving microbubble using uULM. To estimate the parameters describing the problem, the Maximum Likelihood

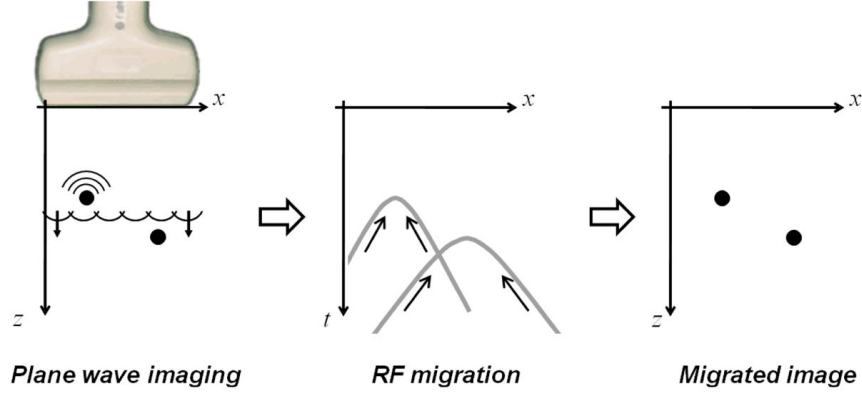


Figure 2.3: Schematic overview of plane wave imaging. [20]

Estimation (MLE) can be used. This method maximizes a likelihood function in such a way that the observed data is most probable under certain statistical assumptions. The point at which this happens is called the Maximum Likelihood Estimator. [21]

2.4.1 The goal of MLE

With the Maximum Likelihood Estimation, the joint probability distribution of random variables $\{d_1, d_2, \dots\}$ can be formulated. These random variables do not have to be identically distributed or independent. [22]

In the formulation of MLE, the vector $\theta = [\theta_1, \theta_2, \dots, \theta_k]^T$ represents the parameters used to index the likelihood function. This is done within a parametric family $\{f(D; \theta) | \theta \in \Theta\}$, in which Θ equals the parameter space. For a given data sample $D = (d_1, d_2, \dots, d_n)$, the joint density results in the following likelihood function L_n : [22]

$$L_n(\theta) = L_n(D; \theta) = f_n(D; \theta) \quad (2.4)$$

If the variables are random distributed and independent, $f_n(D; \theta)$ can be found by multiplying the density functions of each variable. [23]

2.4.2 The Maximum Likelihood Estimate

The maximum likelihood estimate $\hat{\theta} = \hat{\theta}_n(D) \in \Theta$ maximizes L_n and is given by the following equation: [24]

$$\hat{\theta} = \arg \max_{\theta \in \Theta} \hat{L}_n(D; \theta) \quad (2.5)$$

In calculations, often the log-likelihood $\ell(D; \theta) = \ln L_n(D; \theta)$ is used. This $\ell(D; \theta)$ has its maximum at the same position θ as L_n and thus the solution of the maximization problem is not changed. [21], [23]

Assuming $\ell(D; \theta)$ is differentiable in θ , the following likelihood equations formulate certain conditions for the occurrence of a maximum: [22]

$$\frac{\partial \ell}{\partial \theta_1} = 0, \quad \frac{\partial \ell}{\partial \theta_2} = 0, \quad \dots, \quad \frac{\partial \ell}{\partial \theta_k} = 0 \quad (2.6)$$

The maximum likelihood estimate can be used to determine the minimum variance of a certain estimator. This minimum variance is given by the Cramér-Rao Lower Bound, which will be discussed in the next section.

2.5 The Cramér-Rao Lower Bound

To determine the localization precision limits of the microbubble using uULM, one is searching for the minimum standard deviation in the localization of the scatterer. This lower bound on the standard deviation for an unbiased estimator can be derived by the minimum variance, which is given by the Cramér-Rao Lower Bound (CRLB). In this section, a derivation of this CRLB is given.

2.5.1 Fisher Information

The Cramér-Rao Lower Bound theorem states that for a given likelihood function $f(D; \theta)$ with dataset D and parameter θ , the variance for any unbiased estimator $\hat{\theta}$ is given by the following equation: [25]

$$\begin{aligned} \text{var}(\hat{\theta}) &\geq \frac{1}{-E \left[\frac{\partial^2 \ln f(D; \theta)}{\partial \theta^2} \right]} \\ &\geq \frac{1}{\mathcal{I}(\theta)} \end{aligned} \quad (2.7)$$

In above equation, the Fisher Information $\mathcal{I}(\theta)$ is introduced. [26] This matrix is a measure of the amount of information given by an observable random variable D about an unknown parameter θ , which defines the probability of D . [27] The Fisher Information it is given by the following equation:

$$\mathcal{I}(\theta) = -E \left[\frac{\partial^2 \ln f(D; \theta)}{\partial \theta^2} \right] \quad (2.8)$$

In case of the equal sign in equation (2.7), the estimator is said to obey the minimum variance. This CRLB theorem is only valid if the probability distribution $f(D; \theta)$ satisfies the regularity condition, which can be found in equation (2.9). [26]

$$E \left[\frac{\partial \ln f(D; \theta)}{\partial \theta} \right] = 0, \forall \theta \quad (2.9)$$

In some cases, there exists a Minimum Variance Unbiased Estimator (MVUE) $\hat{\theta} = g(D)$, which achieves the CRLB. Such a MVUE exists if and only if the following equation holds: [28]

$$\frac{\partial \ln f(D; \theta)}{\partial \theta} = \mathcal{I}(\theta)(g(D) - \theta) \quad (2.10)$$

The minimum variance CRLB for this parameter can be determined by taking the inverse of the Fisher Information:

$$\text{CRLB} = \mathcal{I}(\theta)^{-1} \quad (2.11)$$

2.5.2 The Fisher Information in case of k parameters

For a dataset D with k parameters, θ will be a vector with size $k \times 1$: $\theta = [\theta_1, \theta_2, \dots, \theta_i, \dots, \theta_{k-1}, \theta_k]^T$. In this case, the Fisher Information will be a $k \times k$ matrix, with the components given by the following (with $i = \{1, 2, \dots, k - 1, k\}$ and $j = \{1, 2, \dots, k - 1, k\}$): [27]

$$[\mathcal{I}(\theta)]_{i,j} = -E \left[\frac{\partial^2}{\partial \theta_i \partial \theta_j} \ln f(D; \theta) \middle| \theta \right] \quad (2.12)$$

Each parameter has its own minimum variance, and thus its own Cramér-Rao Lower Bound. When taking the inverse of the Fisher Information Matrix, the CRLB for each parameter can be found on the diagonal: the minimum variance of parameter i can be found at position (i, i) .

$$\text{CRLB}_{\theta_i} = [\mathcal{I}(\theta)^{-1}]_{i,i} \quad (2.13)$$

The minimum standard deviation can then be determined by taking the squareroot of the minimum variance. [23]

2.5.3 The Efficiency of an Unbiased Estimator

The efficiency of an unbiased estimator indicates how close the estimator variance comes to the CRLB. The estimator efficiency is formulated as:

$$e(\hat{\theta}) = \frac{\mathcal{I}(\theta)^{-1}}{\text{var}(\hat{\theta})} \quad (2.14)$$

Combining equation (2.7) and equation (2.14), one can easily see that $e(\hat{\theta}) = 1$ in case of the CRLB.

With this CRLB, the localization precision limits using uULM can be derived, as will be shown in the next section.

2.6 Localization Precision Limits in uULM

As well as for FPALM, the resolution of uULM is not longer restricted by the diffraction limit. Since the point spread function (PSF) in uULM is highly influenced by the location of the source, it is more complex to determine the maximal achievable resolution compared to FPALM. [9]

The minimum variance of uULM is usually determined in frequency domain: the domain before beamforming. This method is using the parabolas from the Plane Wave Imaging (step b) as introduced in Figure 2.3).

In this research, the maximal achievable resolution is also determined for the beamformed images. In other words, instead of the parabolas, the reconstructed images (as shown in step c) from Figure 2.3) are used for the calculations of the minimum variance. It is interesting to investigate how the RF-based localization precision limits are related to the BF-based ones.

In this section, a general overview of computing the Cramér-Rao Lower Bound in this project will be given. After this, the method will be specified for both the beamformed images (BF-data) and the radiofrequency data (RF-data).

2.6.1 Computing the Cramér-Rao Lower Bound

Now the theory about the imaging method for uULM and the procedure to find the CRLB for different parameters are known, the resulting model for this research can be formulated.

Suppose a detector provides a set of labeled data $D = \{d_{k,t}\}_{k=1,t=1}^{k=K,t=T}$, in which k represents a certain detector pixel, with a total of K and t equals the time. The total detection time equals T .

In this research, the parameters to be estimated are given in the parameter vector $\theta = [\theta_x, \theta_z, I, bg]$, in which θ_x and θ_z represent the localization of the scatterer, I the intensity and bg the background noise. The z -axis is defined to be the direction away from the probe and the x -axis is defined to be colinear to the piezoelectric elements, as shown in Figure 1. To determine the parameters on the entire dataset D , the probability of every measurement has to be computed. This probability is given by the likelihood function f . In the case of microbubbles in blood vessels, all the noises together can be modelled with a white Gaussian noise (WGN). [5] Different sources of noise will be discussed in 2.7. Because of this WGN, the likelihood function is given as: [23]

$$\begin{aligned} f(D; \theta) &= \mathcal{N}(D | \mu, \sigma^2) \\ &= \prod_{k=0, t=0}^{k=K-1, t=T-1} \mathcal{N}(d_{k,t} | \mu_{k,t}, \sigma_{noise}^2) \end{aligned} \quad (2.15)$$

in which $\mu_{k,t}$ equals the expected value of the data without noise for the k -th pixel at time t and σ_{noise}^2 represents the variance of the noise.

As stated before, it is often convenient to use the log-likelihood function for each data point, which is given in (2.16).

$$\ln f(D; \theta) = \sum_{k=0, t=0}^{k=K-1, t=T-1} \ln(\mathcal{N}(d_{k,t} | \mu_{k,t}, \sigma_{noise}^2)) \quad (2.16)$$

The expected value for the k -th detector pixel at time t (indicated with the coordinates $x_{k,t}$ and $z_{k,t}$) is given by $\mu_{k,t}$, which depends on the parameters θ_x , θ_z , the intensity I , the point spread function PSF and the background bg :

$$\mu_{k,t} = I * \text{PSF}(x_{k,t} - \theta_x, z_{k,t} - \theta_z) + bg \quad (2.17)$$

Combining equation (2.17) and equation (2.16), results in the following log-likelihood function: [29]

$$\begin{aligned} \ln f(D; \theta) &= \sum_{k=0, t=0}^{k=K-1, t=T-1} \ln(\mathcal{N}(d_{k,t} | \mu_{k,t}, \sigma_{noise}^2)) \\ &= \sum_{k=0, t=0}^{k=K-1, t=T-1} \ln \left(\frac{1}{\sqrt{2\pi\sigma_{noise}^2}} \cdot \exp \left(-\frac{1}{2} \left(\frac{(d_{k,t} - \mu_{k,t}(\theta))^2}{\sigma_{noise}^2} \right) \right) \right) \\ &= \sum_{k=0, t=0}^{k=K-1, t=T-1} \left(-\frac{1}{2} \ln(2\pi\sigma_{noise}^2) - \frac{1}{2} \left(\frac{(d_{k,t} - \mu_{k,t}(\theta))^2}{\sigma_{noise}^2} \right) \right) \end{aligned} \quad (2.18)$$

With this function, the components of the Fisher Information Matrix can be determined using equation (2.12):

$$\mathcal{I}(\theta_0)_{i,j} = E \left[\left(\frac{\partial}{\partial \theta_i} \ln f(D; \theta) \right) \cdot \left(\frac{\partial}{\partial \theta_j} \ln f(D; \theta) \right) \middle| \theta_0 \right] \quad (2.19)$$

The partial derivative of the log-likelihood with respect to θ_i is given in equation (2.20).

$$\frac{\partial}{\partial \theta_i} \ln f(D; \theta) = \sum_{k=0, t=0}^{k=K-1, t=T-1} \frac{d_{k,t} - \mu_{k,t}(\theta)}{\sigma_{noise}^2} \cdot \frac{\partial \mu_{k,t}(\theta)}{\partial \theta_i} \quad (2.20)$$

Recall that $d_{k,t} = \mu_{k,t} + \text{noise}$. Therefore, $E[(d_{k,t} - \mu_{k,t})^2] = E[(\text{noise})^2] = \sigma_{noise}^2$. [30] The components for the Fisher Matrix will thus reduce to the following:

$$\begin{aligned} \mathcal{I}(\theta_0)_{i,j} &= E \left[\sum_{k=0, t=0}^{k=K-1, t=T-1} \left(\frac{d_{k,t} - \mu_{k,t}}{\sigma_{noise}^2} \right)^2 \cdot \frac{\partial \mu_{k,t}}{\partial \theta_i} \cdot \frac{\partial \mu_{k,t}}{\partial \theta_j} \middle| \theta_0 \right] \\ &= \sum_{k=0, t=0}^{k=K-1, t=T-1} \frac{E[(d_{k,t} - \mu_{k,t})^2 | \theta_0]}{\sigma_{noise}^4} \cdot \frac{\partial \mu_{k,t}}{\partial \theta_i} \cdot \frac{\partial \mu_{k,t}}{\partial \theta_j} \\ &= \sum_{k=0, t=0}^{k=K-1, t=T-1} \frac{1}{\sigma_{noise}^2} \cdot \frac{\partial \mu_{k,t}}{\partial \theta_i} \cdot \frac{\partial \mu_{k,t}}{\partial \theta_j} \end{aligned} \quad (2.21)$$

The partial derivatives of μ with respect to θ are given in the following equations, in which $\text{PSF}_t(x, z)$ represents the point spread function at a given time frame t :

$$\begin{aligned} \frac{\partial \mu_{k,t}}{\partial \theta_x} &= -I \cdot \frac{\partial \text{PSF}_t(x, z)}{\partial x} \bigg|_{(x_k, z_k)} \\ \frac{\partial \mu_{k,t}}{\partial \theta_z} &= -I \cdot \frac{\partial \text{PSF}_t(x, z)}{\partial z} \bigg|_{(x_k, z_k)} \\ \frac{\partial \mu_{k,t}}{\partial I} &= \text{PSF}_t(x_k, z_k) \\ \frac{\partial \mu_{k,t}}{\partial bg} &= 1 \end{aligned} \quad (2.22)$$

By combining equation (2.21) and (2.22), one can see that the minimum variance is independent of the background.

With this information, the Fisher Information Matrix can be determined. As stated before, the minimum variance for each parameter can be found on the diagonal of the inversed Fisher Matrix. By taking the square root of this obtained CRLB, one can find the minimum standard deviation σ . In this research, the precision limits in x - and z -direction for localizing the microbubble are of interest, being respectively:

$$\begin{aligned} \sigma_x &= \sqrt{[\mathcal{I}(\theta)^{-1}]_{1,1}} \\ \sigma_z &= \sqrt{[\mathcal{I}(\theta)^{-1}]_{2,2}} \end{aligned} \quad (2.23)$$

The above derivation for the CRLB can be specified for both the beamformed and the radiofrequency data. The main difference between the two methods is due to the formulation of the PSF and the intensity I as introduced in equation (2.17). To translate the RF-data into readable images, one needs to sum the energy over a backscattered echo and select that value as the pixel intensity for the beamformed image. This process, called beamforming, can be done on the fly or in post-process. Due to this beamforming, the intensity for the RF-data and the BF-data are defined differently. In the next paragraphs, the specifications for both the BF-data and the RF-data will be discussed.

2.6.2 Specifications for the BF-data

Point Spread Function

An imaging process is often modeled as a space-invariant linear system. A point spread function (PSF) is used to describe the imaging system. The image $I(x, z)$ of a certain object $f(x, z)$ can be obtained by computing the convolution of the object with the PSF:

$$I(x, z) = f(x, z) * \text{PSF}(x, z) \quad (2.24)$$

To find the image of the scatterer in the field of view, simulating the microbubble in a blood vessel, it is therefore useful to find the PSF for this situation. In this research, a 1D transducer array is considered. A derivation of the corresponding PSF can be found in the Appendix part A.3, resulting in the following equations:

$$\begin{aligned} \text{PSF}(u, t) &= \max \left| \text{sinc}^2 \left(\frac{a}{\lambda} u \right) \{ \text{pulse}(t) * h_T^P(u, t) * h_R^P(u, t) \} \right| \\ h_T^P(u, t) &= \sum_{n=1}^{N_T} \frac{A_n \delta \left(t - \frac{r_0}{c} - \frac{x_n u}{c} \right)}{r_0} \\ h_R^P(u, t) &= \sum_{m=1}^{N_R} \frac{A_m \delta \left(t - \frac{r_0}{c} - \frac{x_m u}{c} \right)}{r_0} \end{aligned} \quad (2.25)$$

in which $\text{pulse}(t)$ is assumed to be a wideband Gaussian pulse, which covers the whole bandwidth of the array. [31] This pulse is defined as follows (see A.3):

$$\text{pulse}(t) = \begin{cases} g_0 \exp \left[-\frac{\pi^2 \Delta f^2 (t-t_0)^2}{\beta} \right] \sin(2\pi f_0 t) & t \geq 0 \\ 0 & \text{elsewhere} \end{cases} \quad (2.26)$$

For a few simple geometries, one can find the explicit solutions for the PSF as given in equation (2.25). However, since the PSF of a transducer array highly depends on a.o. the depth of the scatterer, the used intensity and the noise, this PSF is usually solved numerically using software like Field II. In [31], it is shown that for a 1D transducer array the PSF obtained with a Field II simulation perfectly overlaps the PSF computed analytically using equation (2.25). To reduce complexity in this research, data from simulation software are used. From the obtained data, the PSF can be determined, as will be explained in Chapter 3. There exist different softwares that can be used to simulate the PSF, for example the Field II [32], SPRITE [33] or WebbPSF [34]. In this research, the Vantage Research Ultrasound Simulator is used because it is easy and fast. [35] The software does not do non-linearities and does not actually simulate a bubble, but is just simulating a sub-wavelength scatterer. However, it will be easy to integrate the performed calculations to any simulation.

Intensity

The intensity for beamformed images is given by the acoustic field, which is measured in decibels (dB). This dynamic range indicates the contrast between noise and the bubble. In ultrasound imaging, a signal is assumed to be visible when its dynamic range is in the order of 20 dB.

2.6.3 Specifications for the RF-data

Point Spread Function

As explained in 2.3.2, the RF-data is a hyperboloid, with its center and shape depending on the position of the source. This hyperboloid represents the time-of-flight as introduced before. Using equation (2.3), the position of the source can be determined, from which the PSF to use in equation (2.17) can be derived. This method will be explained in more detail in Chapter 3.

More about the resolution in frequency domain can be found in the Appendix part A.4. In this section, the spatial error on the reconstructed localization due to the imprecision of the arrival time of the backscattered echo is derived. [9]

Intensity

The RF-data represents what is felt by the transducer array over time. This signal can be measured as an electric signal in arbitrary units, which is proportional to the resulting acoustic pressure in the beamformed images. Remark that the intensity in RF-data is measured linearly, while the intensity in BF-data is measured on a logarithmic scale.

2.6.4 Resulting super-resolution

With the obtained results for the localization precision for both the radiofrequency data and the beamformed images, the resulting super-resolution can be determined. This super-resolution is often expressed as a factor SR , which means that the resolution is improved by a factor SR compared to the wavelength. The classical resolution limit for this problem of a moving microbubble in a blood vessel is given by one wavelength. To determine the resulting super-resolution and the factor SR , one has to divide the wavelength over the obtained minimum standard deviation.

2.7 Sources of Noise

The localization of a microbubble in a blood vessel in real experiments, is subject to large errors. In 2.6, these errors are introduced as σ_{noise} , which contains all the errors together and which is modelled as a zero mean white Gaussian noise. [36] In this section, some of the sources of these noises are discussed.

2.7.1 Sampled Data

Recall that the RF-data represents what is felt by the transducer over time. It is not possible to record continuously what is felt by the piezoelectric element, which is partly due to the amount of generated data. Therefore, the data is sampled and compressed as much as possible. Due to the sampling, the results might deviate slightly compared to continuous data. To minimize this deviation, the Nyquist theorem states that complete information is provided if the sampling rate equals 4 times the transmit frequency. [37]

2.7.2 False Peaks and Jitter

During the measurements and their processing, data is decorrelated by physical processes and corrupted by electronic noise. This could result in an increase of a secondary correlation peak, such that this peak is above the primary correlation peak in amplitude. In this case, one is speaking of so called false peaks. With the use of nonlinear processing, these false peak errors can be minimized. [37] In Figure 2.4, this false peak error is illustrated.

Another type of error is a slight shifting of the peak due to the decorrelation and corruption. This is called jitter, which can be seen in Figure 2.4. All errors too small to be categorized as false peaks, are classified as jitter. Since this type of error can not be removed, it will limit the performance of the position estimation, and thus the localization precision. According to [37], the magnitude of jitter errors can be estimated with Carter's formulation. [38] An in depth derivation of this formulation is out of scope of this research. According [37], the expected jitter when considering blood flow estimations without noise equals 31.1 ns. The resolution when only considering jitter noise varies between 1 nm and 1 μm . [37] Jitter can be approximated as Gaussian noise. [36]

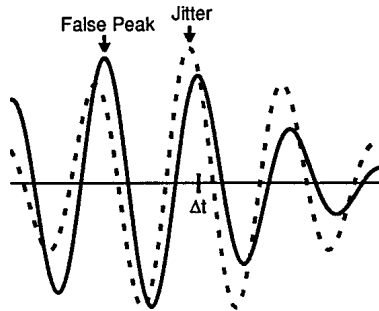


Figure 2.4: RF-data with errors. [37] Δt indicates the position of the peak without any errors. The dashed line equals the data with a jitter error and the solid curve represents the data containing a false peak error.

2.7.3 Readout noise

When measuring the signals, one has to take the limits of physical electronic devices into account as well. A readout detector is used to measure very small packets of charge and on average, this measurement gives the right value for the amount of charge. However, there is some random scatter present as well. When this scatter is measured around the true value, there will be a certain readout noise. For the Verasonics Beamformer, this readout noise equals approximately 10 dB. [39]

2.7.4 Movements

Another important source of error is the motion and the deformation of tissues during in vivo implementation of the microbubble. These movements are difficult to predict or prevent. [9] However, there exist different motion-correcting algorithms, that can compensate for these motions. [40]

Method

In this section, a description of the used method to determine the minimum standard deviations for both the RF-data and the BF-data are given. The calculations and derivations are executed in Matlab. The script can be found in the Appendix part B. By varying the intensity, the behavior of the minimum standard deviation with respect to the intensity can be determined. This process is repeated for different signal-to-noise ratios. The method consists of the following steps:

I. Collect data

For this research, the microbubble is assumed to be a point scatterer moving in a homogeneous medium. The Vantage Research Ultrasound Simulator (Verasonics, Kirkland, WA, USA) is used to simulate a 1D transducer array and a scatterer. Data is provided by a simulation in which the scatterer is moving away from the transducer array, while staying at the same x -position. In 256 time frames, the scatterer moves from $z = 1$ to $z = 26$ mm. For every frame, the obtained beamformed image and the radiofrequency data for that position are stored in a matrix. The RF-data is sampled at 4 times the center frequency of the transducer to ensure Nyquist’s sampling theorem. The coordinates of the scatterer, the BF-data and the RF-data are used in Matlab to determine the localization precision limits of the sub-wavelength microbubble using uULM.

The images are beamformed using Single Crystal High Frequency Transducers from Verasonics, made by Vermon, designed for imaging of small animals and superficial structures. [41] The used probe is a L22-14vX, from which the specifications can be found in Table 3.1. [41]

Center Frequency (MHz)	18.5
Bandwidth (-6 dB)	67 % (avg)
Elements ()	128
Pitch (mm)	0.10
Elevation width (mm)	1.6
Maximum Voltage (V)	± 30
Cable Length (m)	2

Table 3.1: Specifications of the Verasonics L22-14vX. [41]

The used transmit frequency in this research equals 15.625 MHz. The assumed speed of sound is 1540 m/s. With these parameters, one can find that the wavelength equals $\frac{1}{15.625 \cdot 10^6 \text{ s}^{-1}} \cdot 1540 \text{ m/s} \approx 100 \text{ nm}$. The readout noise for this beamformer is assumed to be zero-mean white Gaussian noise

with a variance of 10 dB. [39] For the imaging process in this research, the pixelsize is chosen to be $39.424 \mu\text{m}$ in x -direction and $24.64 \mu\text{m}$ in z -direction.

II. Approximate the PSF

The next step is to approximate the PSF for both the BF-data and the RF-data. The provided data is processed in Matlab 2017b (Mathworks, USA), using the Verasonics beamformer.

BF-data

During the processing of the beamformed data, a pixelsize of $39.424 \mu\text{m}$ in x -direction and $24.64 \mu\text{m}$ in z -direction is used. An example of the beamformed image at a certain time t can be found in Figure 3.1a, in which the intensity in dB is represented as function of the position (x, z) in mm. As one can see, there exists a point of maximum intensity. This is the position at which the scatterer is most likely located at this time t . At this point, the likelihood function achieves its maximum and thus the Cramér-Rao Lower Bound is achieved. .

The areas of less intensities around the peak are side lobes. If there are more scatterers, these side lobes can interfere with each other, resulting in an extra, unwanted point of high intensity. This point would indicate a scatterer at this position, although this is not the case. Therefore, it is important to make a proper approximation for the peak, while neglecting the side lobes. In this research, this approximation is done by the fitting of a one-term Gaussian. The fitting can be seen in Figure 3.1b. First, the BF-data for a certain time frame is loaded and the pixel position (x_k, z_k) of maximum intensity is determined. After this, a cross section is made through this point in x - and in z -direction. An example of such a cross section in z -direction is shown as a dashed line in Figure 3.1c. An one-term Gaussian is then fitted to the cross section to find a point spread function in z -direction, as plotted with the solid line in Figure 3.1c. As one can see, the fitted Gaussian approximates the peak very well, while the side lobes are neglected. This same fitting is done for the cross section in x -direction, to find the PSF in x -direction. By multiplying the point spread function in x -direction with the point spread function in z -direction and normalizing the result, the normalized approximation for the beamformed image is derived. By repeating this process for every time frame t , the PSF for every time can be determined and used in equation (2.17).

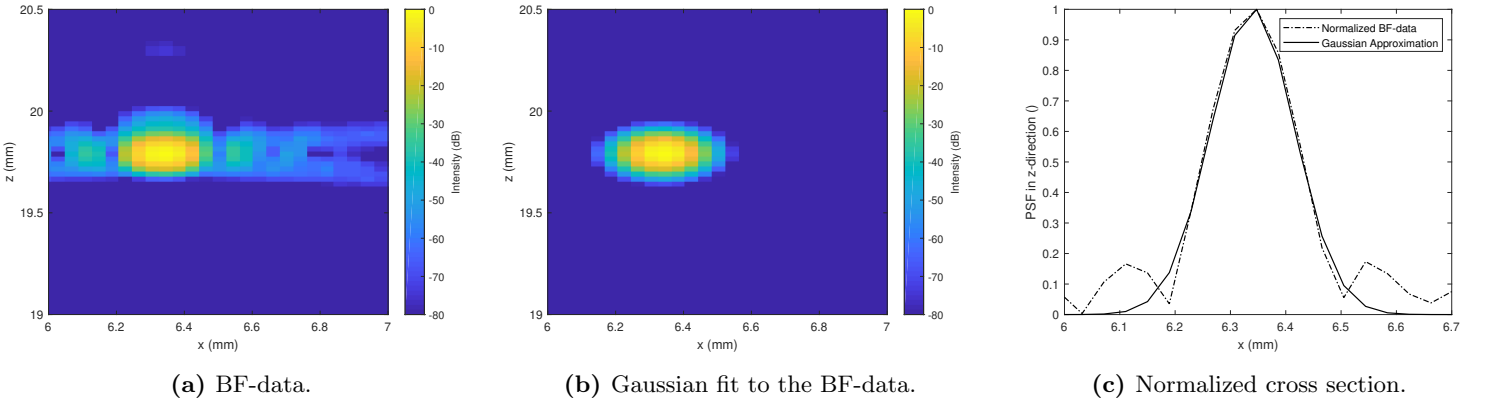


Figure 3.1: The obtained BF-data for the scatterer at a depth of 20 mm, approximated with a Gaussian Fit.

RF-data

The radiofrequency data at a certain time t is shown in Figure 3.2. For the processing, a pitch of 0.10 mm is used. [41] The RF-data represents the time-of-flight as introduced in equation (2.3). To approximate this time-of-flight, one can use a parabola. To find the values for this parabola, first cross sections are made for each transducer elements, as shown in Figure 3.2b and Figure 3.2c. The point of maximum amplitude of these signals is determined and marked in the figures. The corresponding time-of-flights of these points are used to define the parabola. For the two signals as plotted in Figure 3.2b and Figure 3.2c, the points are marked in the RF-data in Figure 3.2d as white dots. This process is repeated for every transducer element, resulting in the points as shown in Figure 3.2e. Using the polyfit function from Matlab2017a to fit a polynomial curve of second order [42], a parabola can be fitted through the points, resulting in the graph as shown in Figure 3.2f.

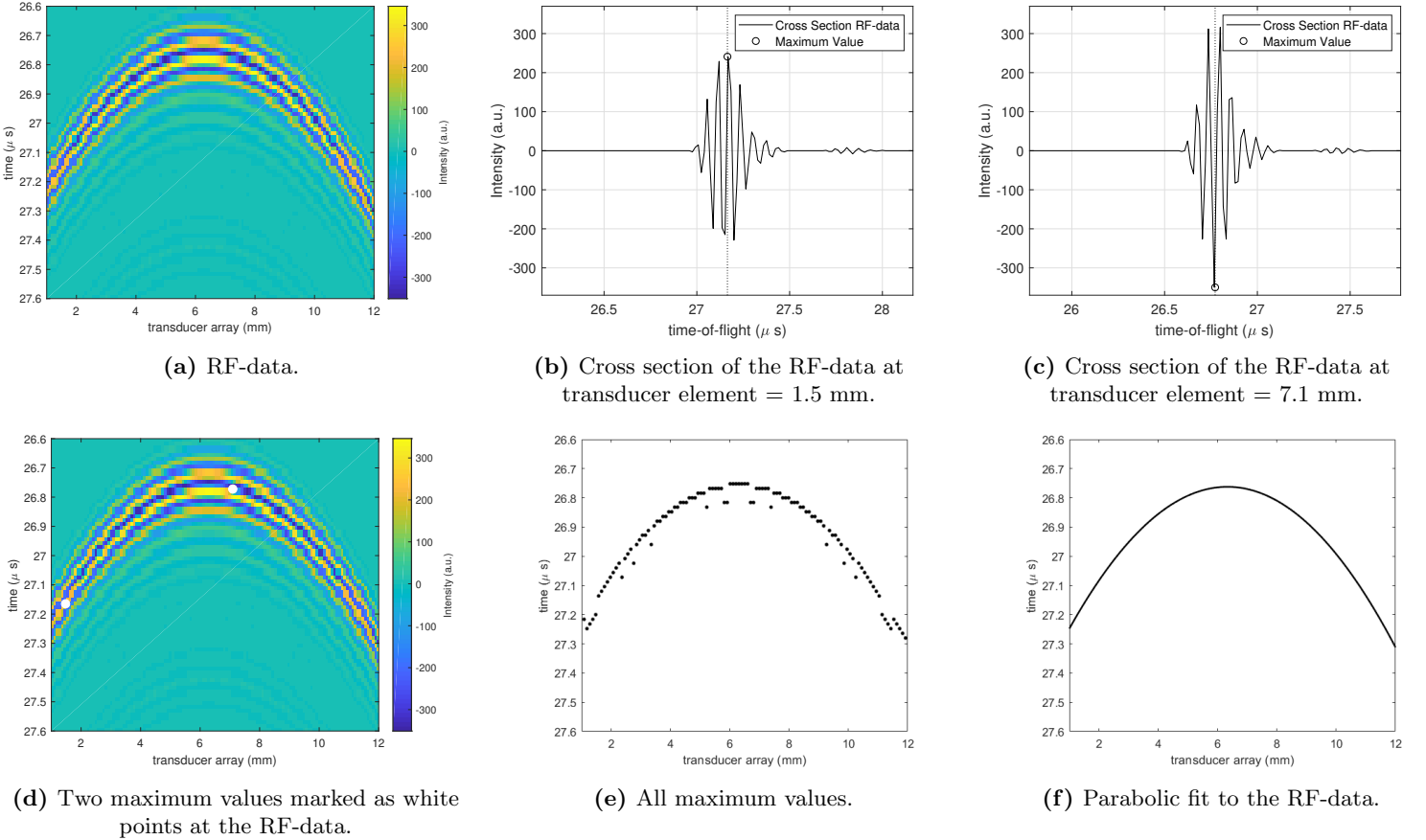


Figure 3.2: The obtained RF-data for the scatterer at a depth of 20 mm, approximated with a parabola.

The pixel (x_k, τ_k) at which the parabola reaches its maximum is stored. With this information, the position of the scatterer can be determined: the x -position can be found by multiplying x_k with the pixelsize in x -direction (being 39 microns): $x = x_k \cdot \text{pixelsize}_x$. The z -position can be determined by looking at the time of flight, which represents the time it takes for the echo to propagate through the medium from the source to the scatterer and back. Dividing this by 2, gives the time it takes to

go from the transducer array to the scatterer. The z -position can then be derived by multiplying this time with the speed of sound c : $z = \frac{1}{2} \frac{\tau_k \cdot c}{4f}$, with $4f$ being the sampling frequency according to the Nyquist rate to convert the pixel number into time.

This procedure to determine the position of the scatterer from the RF-data is repeated for every time frame t . This results in 256 parabolas, each representing the RF-data for the scatterer at a different z -position. These parabolas can be used to derive the point spread function for equation (2.17).

III. Derive the Fisher Information Matrix

With the approximated PSF functions for both the RF-data and the BF-data, one can determine the minimum standard deviation in the localization for both x - and z -direction, using equation (2.22) and equation (2.23), resulting in respectively σ_x and σ_z . As stated before, it is important to use different intensities for the beamformed images and the radiofrequency data. Besides, one has to find a way to determine the derivative in both x - and z -direction for the approximations.

BF-data

In the case of the beamformed image with a Gaussian approximation, the derivatives with respect to x and z can be derived easily by computing the gradient of the Gaussian approximation respectively in x - and z -direction as shown in Figure 3.1b.

RF-data

For the radiofrequency data, the derivative with respect to x is determined by computing the gradient in x -direction of the parabola. Since the z -dependence of the approximation cannot be derived directly from the approximation, the derivative with respect to z is computed using the following equation:

$$\frac{\partial \text{PSF}_t}{\partial z} = \frac{p(t) - p(t-1)}{z(t) - z(t-1)} \quad (3.1)$$

in which $p(t)$ represents the approximated parabola at a certain time frame t and $z(t)$ equals the z -position of the scatterer at a certain time frame t .

IV. Collect more data points

With this information, the minimum standard deviation in x - and z -direction can be determined for both the beamformed images and the radiofrequency data. To collect more data points, steps II and III are repeated for different intensities. Besides, different amounts of noise are added to the data to see what happens with the localization precision limits. Figure 3.3 visualises what happens with the beamformed images if the SNR changes.

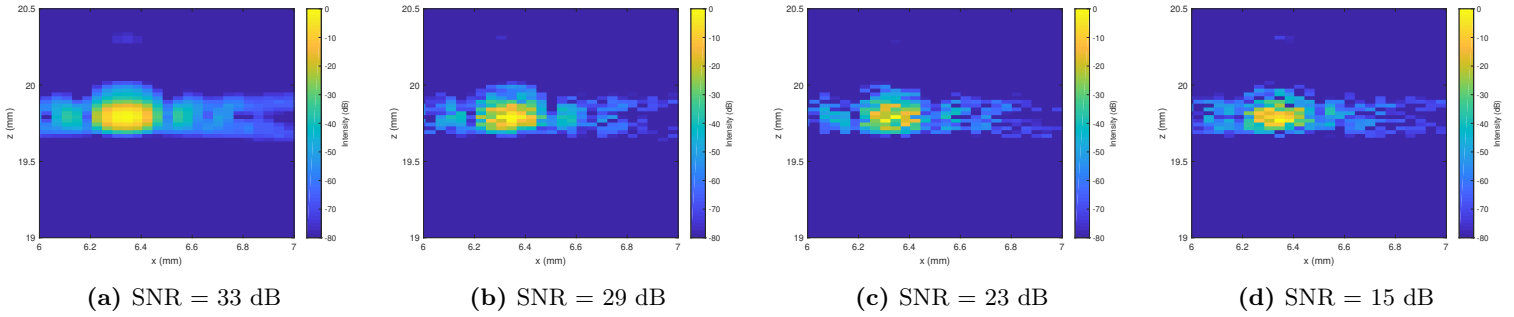


Figure 3.3: BF-data: the obtained images for different signal-to-noise ratios, with the scatterer being positioned at a depth of $z \approx 20$ mm.

For every intensity I and for every SNR, the minimum standard deviations in x - and in z -direction are computed and plotted against the intensity. This way, one can see what happens if the intensity or the signal-to-noise ratio changes.

In the simulation, the intensity in the radiofrequency data varies between 0 and 40 in arbitrary units. The intensity for the beamformed images is chosen to vary between 1 and 40 dB. Both the RF-based and the BF-based localization precision limits are determined for different signal-to-noise ratios, varying between 33 dB, 29 dB, 23 dB and 15 dB.

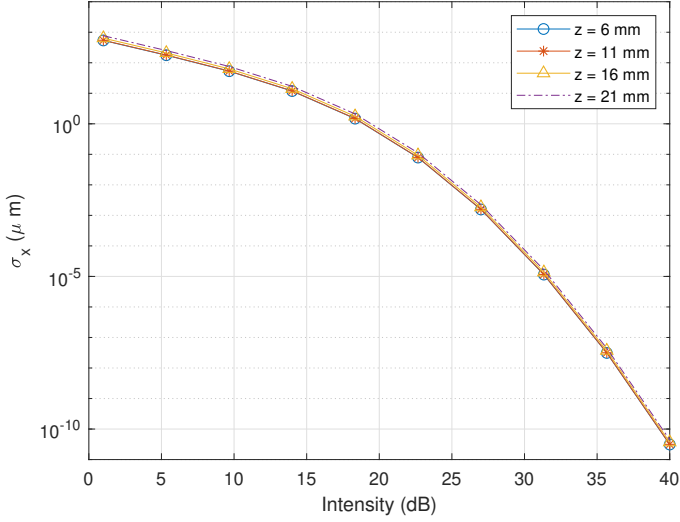
Results & Discussion

In this chapter the results of the precision limits in x - and z -direction for localizing a sub-wavelength microbubble using uULM are evaluated for both the RF-data and the BF-data. First the minimum standard deviation for different depths of the scatterer are given, followed by the results for different SNRs. This chapter will conclude with a discussion of the results and some recommendations for further research.

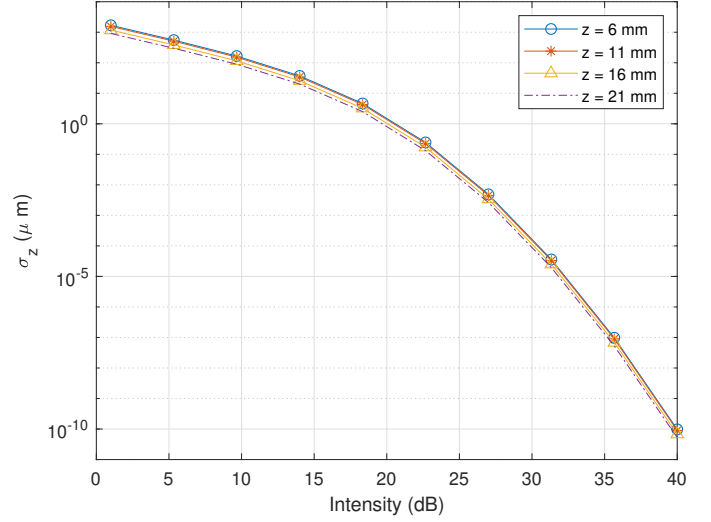
4.1 Localization Precision Limits

4.1.1 Beamformed Images

The localization precision limits σ_x and σ_z for the BF-data determined with the Gaussian Approximations and a signal-to-noise ratio of 23 dB are shown in Figure 4.1. In this graph, the minimum standard deviation in the localization of the scatterer, being the microbubble, is shown. As stated before, the scatterer is moving away from the transducer array in z -direction, which simulates a microbubble moving deeper into a body. The two graphs show the minimum standard deviation in x - and in z -direction for different depths z .



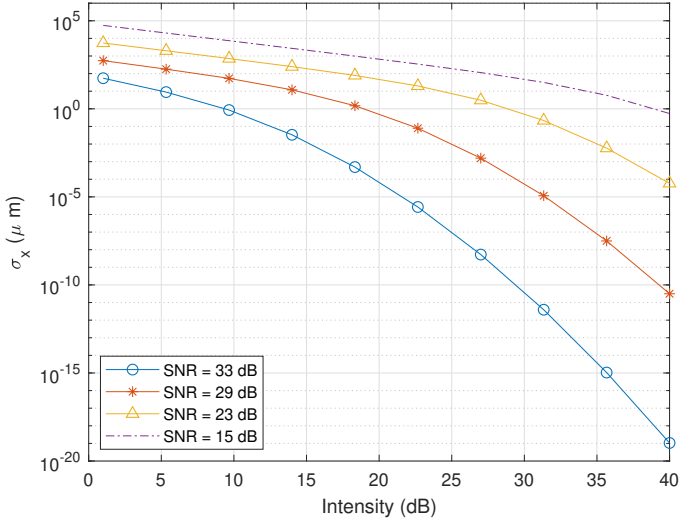
(a) BF-data: σ_x for different depths z .



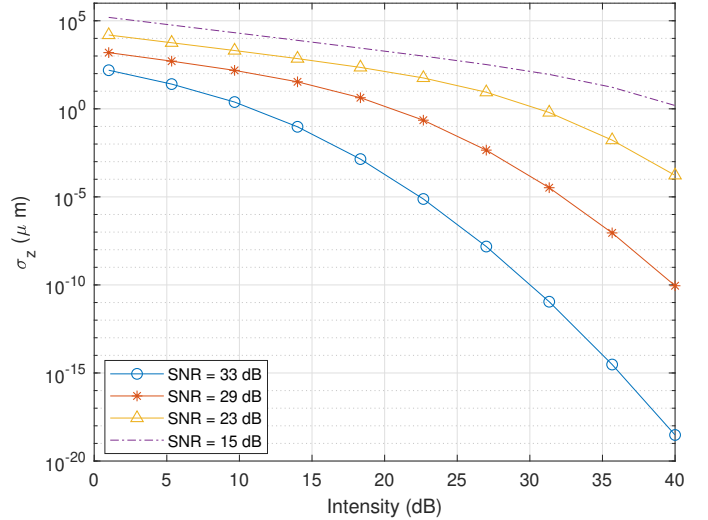
(b) BF-data: σ_z for different depths z .

Figure 4.1: The localization precision limits for the scatterer in both x - and z -direction (respectively σ_x and σ_z) plotted against the intensity (dB) for different depths z , derived from the beamformed images with a SNR of 23 dB.

When changing the amount of noise, the minimum standard deviations will change as well. The behavior of σ_x and σ_z for a scatterer at a depth $z = 11$ mm and a different SNRs can be seen in Figure 4.2.



(a) BF-data: σ_x for different situations of noise.

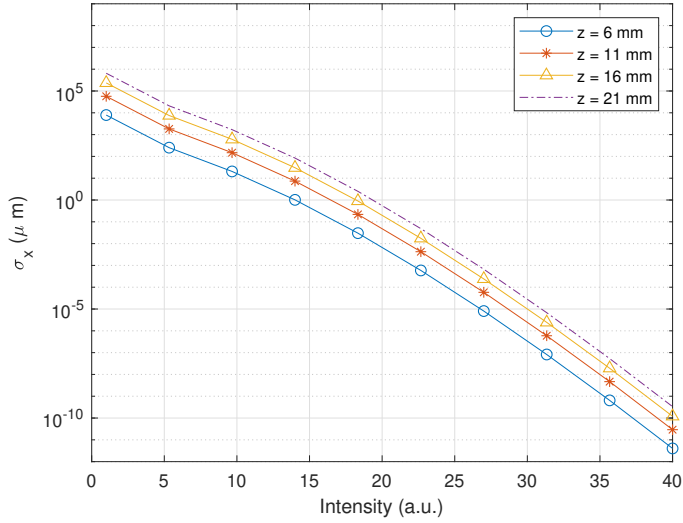


(b) BF-data: σ_z for different situations of noise.

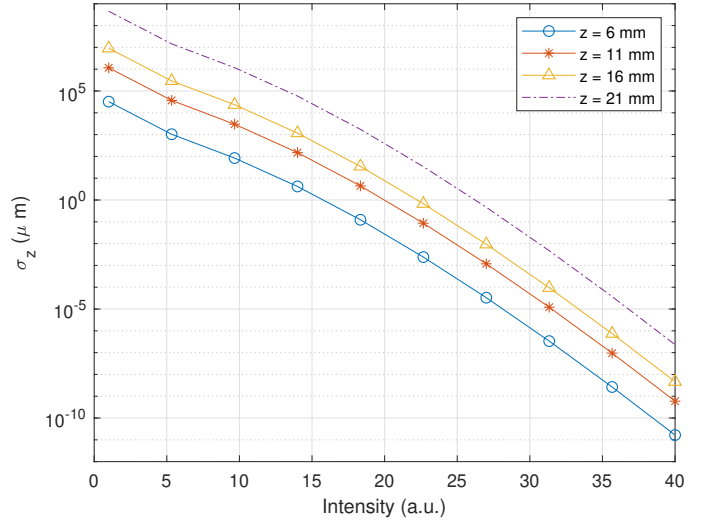
Figure 4.2: The localization precision limits for the scatterer in both x - and z -direction (respectively σ_x and σ_z) plotted against the intensity (dB), derived from the beamformed images. The depth of the scatterer equals 11 mm.

4.1.2 Radiofrequency Data

The same simulations are run for the radiofrequency data: first the localization precision limits are determined for different depths, followed by a comparison between different situations of noise. The minimum standard deviations in the localization for different depths z are shown in Figure 4.3.



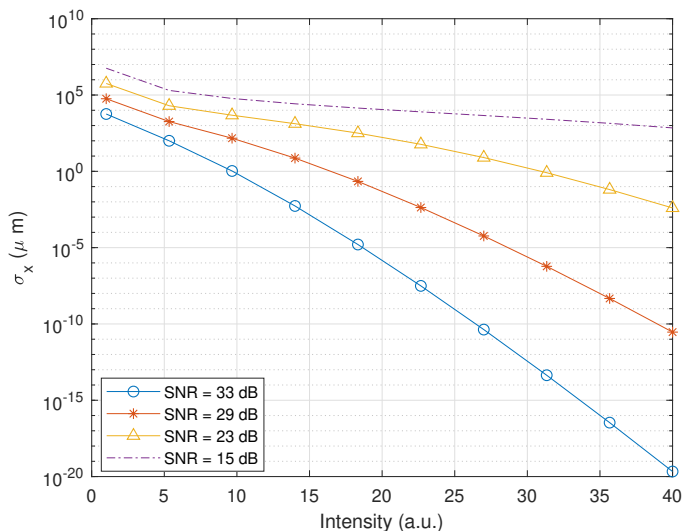
(a) RF-data: σ_x for different depths z .



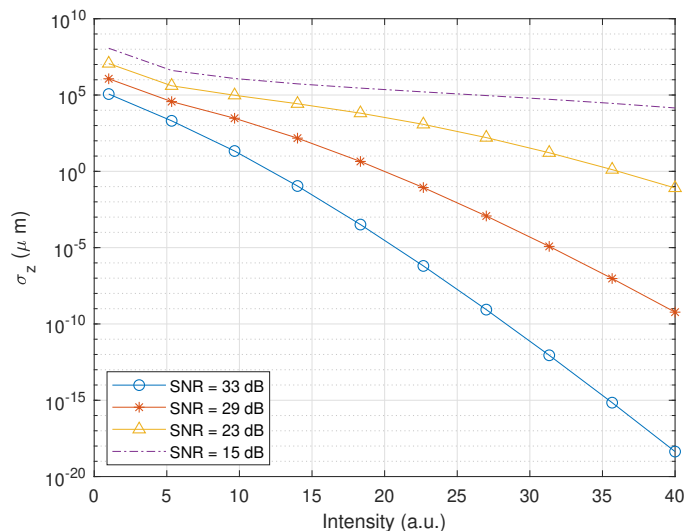
(b) RF-data: σ_z for different depths z .

Figure 4.3: The localization precision limits for the scatterer in both x - and z -direction (respectively σ_x and σ_z) plotted against the intensity (a.u.) for different depths z , derived from the radiofrequency data with a SNR of 23 dB.

The localization precision limits for the RF-data with different situations of noise are shown in Figure 4.4.



(a) RF-data: σ_x for different SNRs.



(b) RF-data: σ_z for different SNRs.

Figure 4.4: The localization precision limits of the scatterer in both x - and z -direction (respectively σ_x and σ_z) plotted against the intensity (a.u.), derived from the radiofrequency data. The depth of the scatterer equals 11 mm.

4.2 Interpretation

Comparing the localization precision for the beamformed images and for the radiofrequency data, results in some remarkable differences.

4.2.1 Variation in Depth

When looking at the localization precision for the RF-data and different depths (see Figure 4.3), one can see that the minimum standard deviation increases when the scatterer is moving away. For a depth of 11 mm, an intensity of 20 a.u. and a SNR of 29 dB, the position of the scatterer can be determined with a precision of 10 nm in x -direction and 50 nm in z -direction. However, for a depth of 21 mm, this precision decreases to 1 μm in x -direction and 0.5 mm in z -direction. This makes sense. To clarify, one could compare this situation with a small light bulb. Suppose there is a sheet of paper between an eye and the light bulb. When the light bulb is moved close to the paper, one can easily determine the shape of the light bulb. However, if one increases the distance between the sheet of paper and the lamp, the exact shape will be harder to distinguish. In other words, the localization precision of the light bulb will be less accurate. This same phenomena happens for the microbubble. When the scatterer is moving deeper into the body, the attenuation of the medium distorts the wavefronts. Therefore, the PSF is distorted as well with increasing depth and the position is harder to estimate in detail. This distortion of PSF is shown in Figure 4.5a. For this graph, the time-of-flight for a certain depth z is divided by its maximum value. This way, the different shapes can be compared easily. As one can see, the position of the peak is less defined for an increasing depth z . Thus, if the microbubble is moving deeper into the body, a higher intensity is needed to achieve the same localization precision. When the microbubble is closer to the transducer array, the localization precision will increase. This means that, for example, following the microbubble through a leg needs a higher intensity than following the bubble in an arm.

So, for the RF-data, it is clear that the localization precision decreases when the microbubble is moving further away. One would expect a similar behavior for the BF-data. However, using the beamformed images, the precision limits are less influenced by the depth of the scatterer, as one can see in Figure 4.1. From these graphs, it becomes clear that there is almost no variation in the localization precision for different depths z . The localization precision approximates $0.5 \mu\text{m}$ in x -direction and $1 \mu\text{m}$ in z -direction for all depths. Looking at the Gaussian approximations for different depths z , results in the graph as shown in Figure 4.5b. Similar to the parabolas from the RF-data, there is a variance in the width of the Gaussian. However, these differences are too small to see a significant difference in the minimum standard deviations in the localization in Figure 4.1.

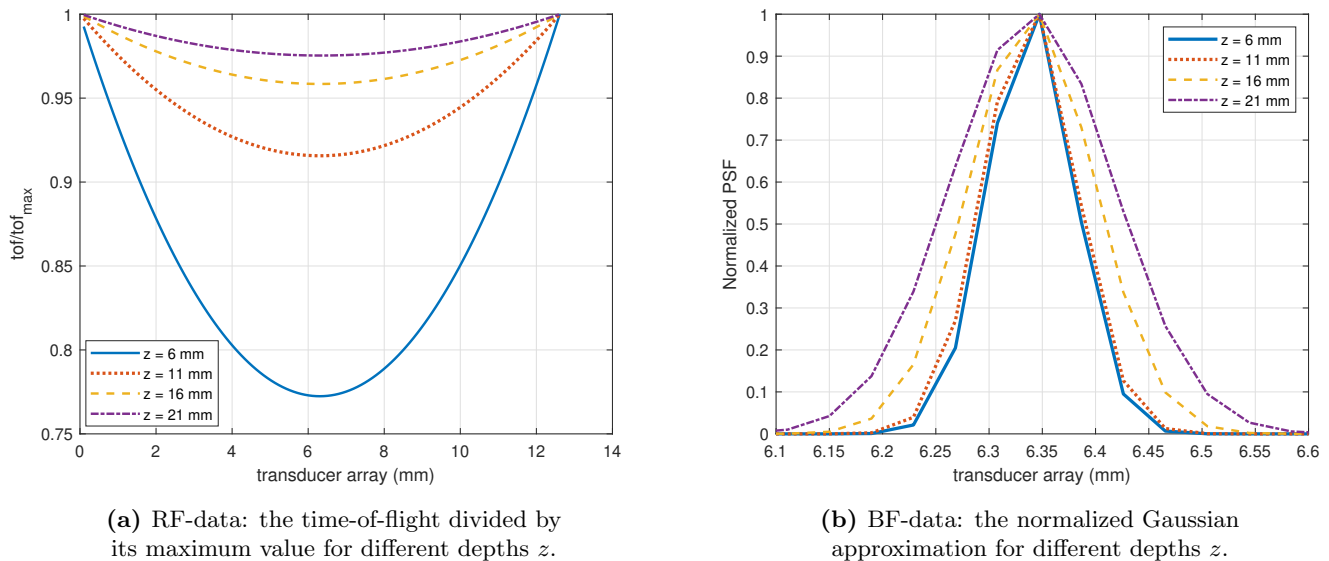


Figure 4.5: The approximations for different depths z for both the radiofrequency and the beamformed images.

A remarkable result is that the minimum standard deviation is way higher for the RF-based localization compared to the BF-based localization. However, after a certain depth, the localization precision limits obtained with the beamformed images surpass the limits obtained with the radiofrequency data. This is due to the RF-migration, as explained in 2.3.2. Since the energy of the whole parabola is concentrated into one pixel by the migration, the signal-to-noise ratio is higher in the beamformed images compared to the radiofrequency data.

The beamforming step, in which the RF-data is converted into images, will thus influence the localization precision. Comparing the RF-based minimum standard deviation with the BF-based precision is comparing apples and oranges. The initial values for this beamforming process, a.o. the SNR and the maximum intensity, are difficult to compare for the RF-data and the BF-data. For example, the amount of energy between the radiofrequency data and the beamformed images is not consistent, which makes it very difficult to compare the intensity between the two sets. Besides, the geometry of the point spread function differs, since the localization step consists in determining the centroid of the PSF beyond the diffraction limit. The detailed process of beamforming is complex and out of scope of this project. However, it is based on some assumptions which are not completely correct. In further research, it is useful to take a closer look into the beamforming. One should investigate how to convert the intensity in arbitrary units from the radiofrequency data

into the intensity in decibels for the beamformed images. With this conversion, a better comparison between the localization precision limits in RF-data and in BF-data can be made. Besides, algorithms should be adapted such that they take into account the difference in SNR between the BF-data and the RF-data and perform a two-step localization.

4.2.2 The Influence of Noise

As one can see in Figure 4.2 and 4.4, the localization precision limits are similarly influenced by the noise for the RF-data and the BF-data in both x - and z -direction. Looking at the overview of the beamformed images under different situations of noise as shown earlier in Figure 3.3, the expectation arises that the localization precision limits will decrease if the amount of noise increases. This is confirmed by the graphs as shown in Figure 4.2 and Figure 4.4: for the radiofrequency data, for example, using the same intensity and depth, a localization precision in x -direction of 1 nm can be achieved for a SNR of 33 dB, while a SNR of 23 dB results in a precision of 10 mm. It is, therefore, desirable to minimize the noise during the localization process. This can be done by, for example, using electronic devices with less readout noise, by the implementation of motion-correcting algorithms or by using nonlinear processing to minimize the false peak errors as explained before in 2.7.

4.3 Resulting super-resolution

With the above results for the localization precision limits for both the radiofrequency data and the beamformed images, the resulting super-resolution can be determined. The classical resolution limit for this problem is given by one wavelength; being approximately $100 \mu\text{m}$. The median diameter of a microbubble contrast agent is assumed to be $3 \mu\text{m}$. An entire overview of the super-resolution factor SR for the different intensities and the different SNRs can be found in Table 6.1 and Table 6.2 in the Supplementary Data. Some of the results for the BF-data and the RF-data are illustrated in respectively Figure 4.6 and Figure 4.7.

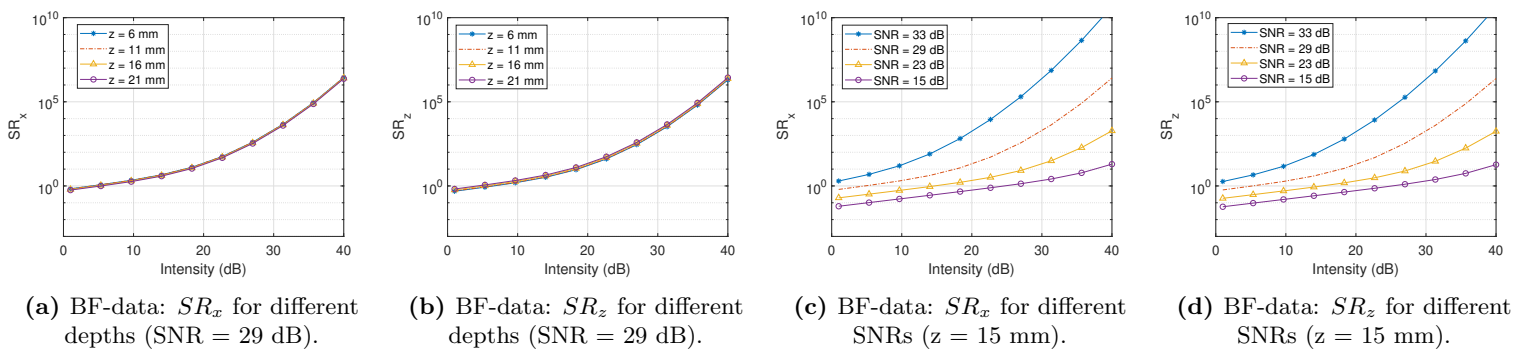


Figure 4.6: The resulting super-resolution in both x - and z -direction obtained with the beamformed images for different depths z or different signal-to-noise ratios SNR.

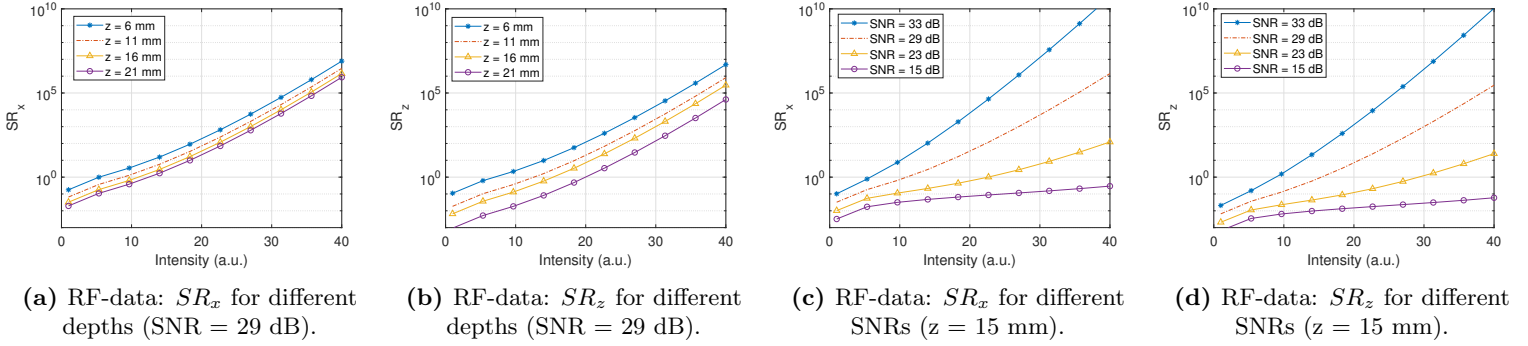


Figure 4.7: The resulting super-resolution in both x - and z -direction obtained with the radiofrequency data for different depths z or different signal-to-noise ratios SNR.

In medical applications, a transmit frequency of 15 MHz is typically used to scan biological tissues up to 2 cm deep. Beyond that distance, the attenuation starts to be prominent and the SNR is not sufficient anymore for imaging. In this research, the BF-based localization precision limits are way lower and the super-resolution way higher compared to the RF-data. Besides, the signal-to-noise ratio is higher in the beamformed images due to the RF-migration. Therefore, it seems better to use the BF-data for the localization. However, it is risky to compare the results and decide which data set should be used to localize the microbubble because of the beamforming step. As stated before, the initial values for this process are difficult to define, which makes a comparison for the obtained results ungrounded. Before comparing, the conversion of the measured voltages into the intensity in the final images should be investigated and the algorithms should be adapted into a two-steps localization. After these modifications, the results can be compared properly and one can decide which data set is preferably used in the localization of the scatterer.

4.4 Further Recommendations

Apart from the recommendations to minimize the noise, to study the beamforming step and to adapt the algorithms into a two-step localization, there are some more aspects to investigate in further research.

4.4.1 Approximations

In this research, the radiofrequency data is approximated with a 1D-parabola, as shown in Figure 3.2f. With this approximation, however, some information from the RF-data is lost. For example, the derivative in z -direction is now computed using equation (3.1). When fitting a 3D-function to the RF-data instead of a parabola, this derivative could be determined more precisely. One way to do this 3D-fitting is by using the Cubic Spline Data Interpolation Function in Matlab. With this function, one can obtain a vector of interpolated values corresponding to certain query points, using cubic spline interpolation. [43] One advantage of this Spline approximation is the fact that the first and second derivative are continuous. However, the Spline approximation is that accurate that it takes into account all the noises in the image as well. In further research, one has to find a way to approximate the peak values with a Spline function, without including the noise.

This same recommendations goes for the BF-data: in this research, the beamformed images are approximated with a 2D-Gaussian, as shown in Figure 3.1b. The BF-data, however, is given as a 4D-function, depending on the intensity, the background, the x -position and the depth z . It would be interesting to see what happens with the localization precision limits if the beamformed images are approximated with a 4D-function.

The radiofrequency signals are measured voltages, oscillating around zero. An example of such a signal can be found in Figure 4.8. During the process of beamforming, only the envelope of this signals is used, which means that only the positive values are taken into account and the negative values are neglected. Another method to increase the reliability of the localization precision, is by using the whole signals, and not just the envelopes of the RF-data.

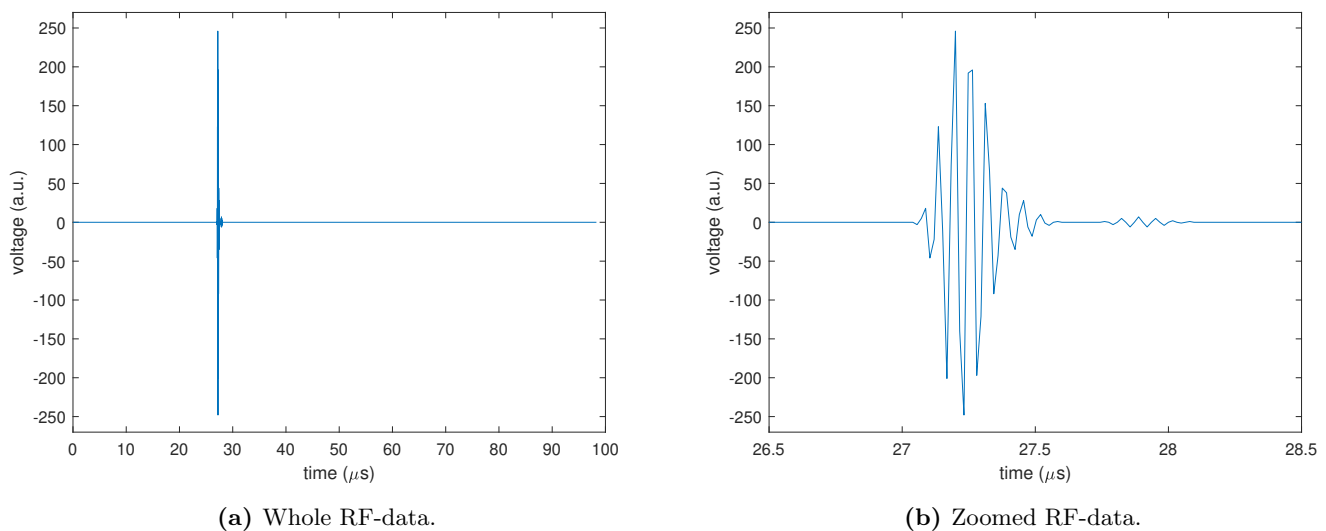


Figure 4.8: The RF-data for a single transducer.

4.4.2 Increasing the range of measurements

Suppose a small object is positioned at 40 m from a person. When moving this object closer to this man, he will be able to see the object sharply. However, at some point, the person is not able to see the details anymore, because it has moved too close to his eye. There seems to be a relation between the sharpness of the object and the distance to the person. When starting very close to an eye, and moving away from it, the sharpness will increase, come to a maximum and then decrease again. In optics, these different regions are indicated as the Fraunhofer Region for the far-field approximation and the Fresnel Region for the near-field approximation. [44], [45]

This same difference between the far field and the near field occurs for the microbubble and its localization precision limits. When the scatterer is too close to the transducer array, the backscattered echo will not hit all transducer elements and thus not use the whole array, but just a sub-aperture. If the microbubble is moving further away, more elements receive the backscattered echo and the resolution will improve. However, when increasing this distance even more, there will be more attenuation through the material, which will decrease the resolution again. In further research, it would be interesting to map the whole imaged space with sub-wavelength displacements in both the

x - and z -direction. After a certain depth, the signal-to-noise ratio will be too low to perform the localization properly. It is interesting to determine this depth, to make sure that this distance will not be exceeded during medical applications. Besides, instead of assuming a point like scatterer, one could try to run the simulation for a little sphere with a radius of $3 \mu\text{m}$, approximating the shape of a real microbubble.

4.4.3 The Grid

During beamforming, the radiofrequency data is converted into images. As explained in 2.3.2, the RF-data is measured as an electric signal. The parabolas are the truncated spherical waves, scattered back from the point like scatterers. For the conversion of RF-data into images, first the acoustic pressure along a certain parabola is summed to one value. This value is used to determine the intensity in a pixel in the final image. After all pixels are done, the intensity in each pixel is divided by the maximum intensity and converted to decibels. This results in the final beamformed image.

In other words; the final image is divided into a grid in which each pixel corresponds to a certain parabola from the RF-data. Therefore, the summed parabolas depends on the grid in the final image and thus it is important to choose this grid properly.

In further research, it would be useful to determine the localization precision limits in both the RF-data and the BF-data using different grids in the beamformed image. This way, the relation between the chosen grid, the localization precision in RF-data and the localization precision in BF-data can be visualised. It could be that the chosen grid in this research is not suitable for this problem, which could explain the difference in the minimum standard deviations obtained for the RF-data and the BF-data. This however, lacks in the state of the art, as most scientist tend to compare beamformer precision through signal-to-noise ratio measurements in simulated data, and not through signal analysis.

4.4.4 Position of the Scatterer

In this research, there are three different data files from which the position of the scatterer can be determined:

- **The Beamformed Images:** the location of the maximum intensity in the beamformed images represents the position of the scatterer.
- **The Radiofrequency Data:** from the fitted parabola on the time-of-flight, the position of the scatterer can be determined.
- **The MediaCoordinates:** during the simulation, the position of the scatterer is stored in a matrix.

Plotting these three coordinates together, results in the graph as shown in Figure 4.9. As one can see, the point of maximum intensity in the beamformed image is almost equal to the position according the radiofrequency data, but they do not exactly overlap. This is due to inhomogeneities in the PSF. In further research, it might be interesting to take these inhomogeneities into account while approximating the PSF, to make sure that the maximum intensity and the location according the time-of-flight are at the same position. The stored position according the MediaCoordinates

are at a total different location compared to the point of maximum intensity and the position according the time-of-flight. The deviation in x -direction is due to shifting and is not important in this research. However, also the z -positions show a difference compared to the other two data sets. According the MediaCoordinates, the scatterer is moving less far (the curve is much shorter), but at a deeper location (the curve is much higher) compared to the RF-data and the BF-data. This does influence the localization precision for the different depths.

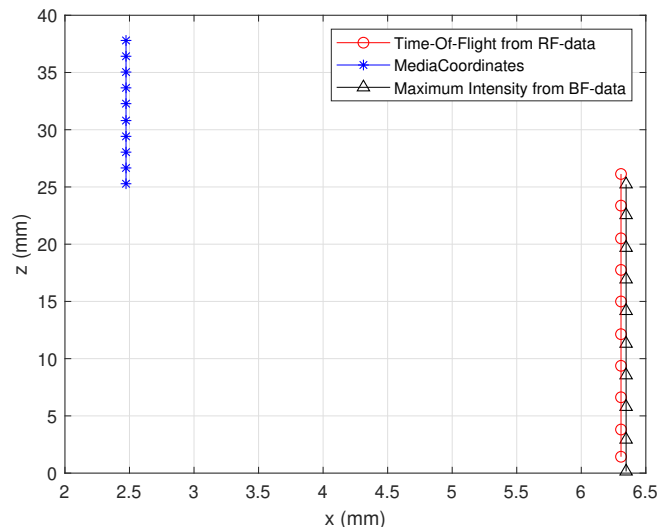


Figure 4.9: The position of the scatterer according the different data types.

Since the data was provided, the cause of the different positions for the scatterer according the MediaCoordinates, the beamformed images and the radiofrequency is unknown. With the MediaCoordinates, only 128 positions are given, while there are twice as much images (and thus 256 positions) for the BF-data and RF-data. Besides, it is important to check the exact depth of the scatterer. In this research, the positions determined with the time-of-flight are taken as default for the derivation of the localization precision in the radiofrequency data. For the beamformed images, the position of the maximum intensity is used. The difference in z -direction between these positions is negligible in the discussion of the results and might be caused by the error as derived in the Appendix part A.4. This difference can be minimized by using probes with a higher sensitivity.

When using the coordinates as provided by the data MediaCoordinates as default in the calculations, all depths (for example the depths as given in the legend in Figure 4.1, Figure 4.3 and Figure 4.5) will change. Besides, the derivation of the z -derivative using equation (3.1) will change as well, resulting in a slightly different localization position. In further research, it would be good to simulate all values again, while providing just as much coordinates as images. Besides, it would be good to take the inhomogeneities of the tissues into account as well. These inhomogeneities should be corrected before localization.

Conclusion

This research has investigated the theoretical precision limit of ultrafast Ultrasound Localization Microscopy (uULM) in localizing a moving sub-wavelength scatterer. In essence, the process of acoustic imaging in uULM consists of three steps: the plane wave transmission, the reception of the backscattered echoes (measured as an electric signal, denoted as the radiofrequency data or RF-data) and the image reconstruction (resulting in the beamformed images or BF-data). In this research, the localization precision limits for both the (RF-data) and the BF-data are determined.

With this investigation a difference in the localization precision limits considering different depths of the scatterer using radiofrequency data or using beamformed images is revealed. According to the RF-data, the minimum standard deviation decreases if the scatterer moves away to a deeper position: for a depth of 11 mm, the position of the scatterer can be determined with a precision of 10 nm in x -direction and 50 nm in z -direction, while this decreases to 1 μm in x -direction and 0.5 mm in z -direction at a depth of 21 mm, using the same intensity and with the same SNR. Thus, if the microbubble is moving deeper into the body, a higher intensity is needed to achieve the same localization precision. When the microbubble is closer to the transducer array, the localization precision will increase.

This z -dependence was less obvious in the BF-data. At an intensity of 20 dB and a SNR 29 dB, the localization precision approximates 0.5 μm in x -direction and 1 μm in z -direction for all depths. A remarkable result is that the localization precision limits using the radiofrequency data is way higher compared to the beamformed images. However, after a certain depth, the BF-based localization surpasses the RF-based one. The differences between the results obtained with the RF-data and the BF-data are due to the beamforming step. The SNR and the maximum intensity for this process are difficult to define and compare for the RF-data and BF-data.

The RF-based and BF-based localization precision react similar to changes in the amount of noise. For a low signal-to-noise ratio, the position of the scatterer can be determined with a lower precision compared to a situation with a high signal-to-noise ratio. For the radiofrequency data, for example, using the same intensity and depth, a localization precision in x -direction of 1 nm was obtained for a SNR of 33 dB, while a noise of 23 dB resulted in a precision of 10 mm.

Due to the influence of the beamforming step, it is difficult to determine from above results which set should be used for the localization of a microbubble in medical applications. In further research, it is therefore useful to investigate the beamforming step in detail. It is, for example, interesting to see how the intensity in the radiofrequency is related to the intensity in the beamformed images. In addition, uULM researchers should adapt their algorithm to perform a two-step localization,

compensating for the RF-migration. This way, one is able to compare the BF-based and RF-based results properly. Besides, it is interesting to increase the range of measurements, to see what happens if the microbubble is moving deeper into the body, or closer to the transducer array. Lastly, one could approximate the RF-data and BF-data with other functions. Using 3D-approximations, less information is lost and the derivatives, for example, can be determined more accurately.

- [1] G. Montaldo, M. Tanter, J. Bercoff, N. Benech, and M. Fink, “Coherent plane-wave compounding for very high frame rate ultrasonography and transient elastography,” *IEEE Transactions on Ultrasonics, Ferroelectrics, and Frequency Control*, vol. 56, no. 3, pp. 489–506, 2009.
- [2] Wikipedia contributors, “Microscopy — Wikipedia, the free encyclopedia.” <https://en.wikipedia.org/w/index.php?title=Microscopy&oldid=959451279>, 2020. [Online; accessed 8-June-2020].
- [3] Wikipedia contributors, “Photoactivated localization microscopy — Wikipedia, the free encyclopedia.” https://en.wikipedia.org/w/index.php?title=Photoactivated_localization_microscopy&oldid=951352572, 2020. [Online; accessed 7-May-2020].
- [4]
- [5] O. Couture, V. Hingot, B. Heiles, P. Muleki Seya, and M. Tanter, “Ultrasound localization microscopy and super-resolution: A state of the art,” *IEEE Transactions on Ultrasonics, Ferroelectrics, and Frequency Control*, vol. PP, pp. 1–1, 06 2018.
- [6] A. A. H.P. Urbach and A. Konijnenberg, *Optica Lecture Notes*. TN2421, Delft University, 2020.
- [7] D. Birkett, “Numerical aperture - don keuth,” 2013.
- [8] Joel S. Silfies, Stanley A. Schwartz, Micheal W. Davidson, “The diffraction barrier in optical microscopy — Nikon, microscopy u, the source for microscopy education.” <https://www.microscopyu.com/techniques/super-resolution/the-diffraction-barrier-in-optical-microscopy>, 2020. [Online; accessed 23-April-2020].
- [9] Y. Desailly, J. Pierre, O. Couture, and M. Tanter, “Resolution limits of ultrafast ultrasound localization microscopy,” *Physics in Medicine and Biology*, vol. 60, pp. 8723–8740, oct 2015.
- [10] S. Hess, T. Girirajan, and M. Mason, “Ultra-high resolution imaging by fluorescence photoactivation localization microscopy,” *Biophysical journal*, vol. 91, pp. 4258–72, 01 2007.
- [11] The University of Maine, “Fluorescence photoactivation localization microscopy (fpalm).” <https://physics.umaine.edu/research/biophysics-research-group/fpalmhome/fpalmoverview/>, 2020. [Online; accessed 24-April-2020].
- [12] S. Hess, T. Gould, S. Gunewardene, J. Bewersdorf, and M. Mason, *Ultrahigh Resolution Imaging of Biomolecules by Fluorescence Photoactivation Localization Microscopy*, vol. 544, pp. 483–522. 02 2009.

- [13] Wikipedia contributors, “Photobleaching — Wikipedia, the free encyclopedia.” <https://en.wikipedia.org/w/index.php?title=Photobleaching&oldid=934378496>, 2020. [Online; accessed 24-April-2020].
- [14] J. Bewersdorf, “Advances in super-resolution biplane fpalm, sted and 3d particle tracking microscopy,” 04 2011.
- [15] N. Bobroff, “Position measurement with a resolution and noise-limited instrument,” *Review of Scientific Instruments*, vol. 57, pp. 1152 – 1157, 07 1986.
- [16] C. Errico, J. Pierre, S. Pezet, Y. Desailly, Z. Lenkei, O. Couture, and M. Tanter, “Ultrafast ultrasound localization microscopy for deep super-resolution vascular imaging,” *Nature*, vol. 527, no. 7579, pp. 499–502, 2015.
- [17] L. Demi, “Practical guide to ultrasound beam forming: Beam pattern and image reconstruction analysis,” *Applied Sciences*, vol. 8, p. 1544, 09 2018.
- [18] L. Tong, H. Gao, H. F. Choi, and J. D’hooge, “Comparison of conventional parallel beam-forming with plane wave and diverging wave imaging for cardiac applications: a simulation study,” *IEEE Transactions on Ultrasonics, Ferroelectrics, and Frequency Control*, vol. 59, no. 8, pp. 1654–1663, 2012.
- [19] T. Ahlersmeyer, *Advanced experimental techniques in vehicle noise and vibration refinement*, pp. 189–216. 12 2010.
- [20] D. Garcia, L. Le Tarneç, S. Muth, E. Montagnon, J. Porée, and G. Cloutier, “Stolt’s f-k migration for plane wave ultrasound imaging,” *Ultrasonics, Ferroelectrics and Frequency Control, IEEE Transactions on*, vol. 60, pp. 1853–1867, 09 2013.
- [21] Jonny Brooks-Bartlett, “Probability concepts explained: Maximum likelihood estimation — Towards Data Science,” 2018, January 4th.
- [22] Wikipedia contributors, “Maximum likelihood estimation — Wikipedia, the free encyclopedia.” https://en.wikipedia.org/w/index.php?title=Maximum_likelihood_estimation&oldid=950319146, 2020. [Online; accessed 21-April-2020].
- [23] F. Dekking, C. Kraaikamp, H. Lopuhaä, and L. Meester, *A Modern Introduction to Probability and Statistics: Understanding Why and How*. Springer Texts in Statistics, Springer, 2005.
- [24] P. S. H. Chan, *Lecture 8: Properties of Maximum Likelihood Estimation (MLE)*. ECE 645: Estimation Theory, Purdue University, 2015, April 27.
- [25] Tampere University of Technology, “Cramer-rao lower bound.” <http://www.cs.tut.fi/~hehu/SSP/lecture2.pdf>. [Online; accessed 21-April-2020].
- [26] J. Duchi, *Lecture Notes for Statistics 311/Electrical Engineering 377*. Stanford University, 2019, March 7.
- [27] Wikipedia contributors, “Fisher information — Wikipedia, the free encyclopedia.” https://en.wikipedia.org/w/index.php?title=Fisher_information&oldid=957425590, 2020. [Online; accessed 26-May-2020].
- [28] C. Smith, N. Joseph, B. Rieger, and K. Lidke, “Fast, single-molecule localization that achieves theoretically minimum uncertainty,” *Nature methods*, vol. 7, pp. 373–5, 04 2010.

- [29] F. Rusek, *Estimation Theory*. European Institute of Innovation Technology.
- [30] E. W. Weisstein, “Normal distribution.”
- [31] Z. Li and C. Chi, “Fast computation of far-field pulse-echo psf of arbitrary arrays for large sparse 2-d ultrasound array design,” *Ultrasonics*, vol. 84, pp. 63–73, 2018.
- [32] J. A. Jensen, Apr 2019.
- [33] F. Ngole, “Sprite,” Jun 2017.
- [34] STScI, “Psf simulation tool,” Oct 2019.
- [35] Verasonics, “The verasonics research ultrasound simulator – an innovative tool for verification of programming protocols.” <https://verasonics.com/ultrasound-simulator/>, 2020. [Online; accessed 27-June-2020].
- [36] M. J. Underhill and P. J. Brown, “Estimation of total jitter and jitter probability density function from the signal spectrum,” in *2004 18th European Frequency and Time Forum (EFTF 2004)*, pp. 502–508, 2004.
- [37] W. F. Walker and G. E. Trahey, “A fundamental limit on delay estimation using partially correlated speckle signals,” *IEEE Transactions on Ultrasonics, Ferroelectrics and Frequency Control*, vol. 42, pp. 301–308, 1995.
- [38] G. C. Carter, “Coherence and time delay estimation,” *Proceedings of the IEEE*, vol. 75, no. 2, pp. 236–255, 1987.
- [39] Y. Qi, Y. Wang, J. Yu, and Y. Guo, “Short-lag spatial coherence imaging using minimum variance beamforming on dual apertures,” *Biomedical engineering online*, vol. 18, no. 1, p. 48, 2019.
- [40] B. Denarie, T. A. Tangen, I. K. Ekroll, N. Rolim, H. Torp, T. Bjåstad, and L. Lovstakken, “Coherent plane wave compounding for very high frame rate ultrasonography of rapidly moving targets,” *IEEE Transactions on Medical Imaging*, vol. 32, no. 7, pp. 1265–1276, 2013.
- [41] “Vermon single crystal high frequency linear arrays,” Apr 2020.
- [42] “polyfit.”
- [43] “spline.”
- [44] Wikipedia contributors, “Fraunhofer diffraction — Wikipedia, the free encyclopedia.” https://en.wikipedia.org/w/index.php?title=Fraunhofer_diffraction&oldid=955701940, 2020. [Online; accessed 21-June-2020].
- [45] Wikipedia contributors, “Fresnel equations — Wikipedia, the free encyclopedia.” https://en.wikipedia.org/w/index.php?title=Fresnel_equations&oldid=963593363, 2020. [Online; accessed 21-June-2020].
- [46] A. B. Forming, “Chapter 3 antenna arrays and beamforming.”
- [47] Wikipedia contributors, “Beamforming — Wikipedia, the free encyclopedia.” <https://en.wikipedia.org/w/index.php?title=Beamforming&oldid=943058100>, 2020. [Online; accessed 23-April-2020].

- [48] C. Dalitz, R. Pohle-Frohlich, and T. Michalk, “Point spread functions and deconvolution of ultrasonic images,” *IEEE Transactions on Ultrasonics, Ferroelectrics, and Frequency Control*, vol. 62, no. 3, pp. 531–544, 2015.
- [49] Q. Wang, N. Guo, H. Du, and W. Huang, “Beam pattern calculation for optimization of broadband array transducers,” *The Journal of the Acoustical Society of America*, vol. 120, no. 2, pp. 741–749, 2006.
- [50] J. W. Hunt, M. Arditi, and F. S. Foster, “Ultrasound transducers for pulse-echo medical imaging,” *IEEE Transactions on Biomedical Engineering*, no. 8, pp. 453–481, 1983.
- [51] C. Chi and Z. Li, “Fast computation of wideband beam pattern for designing large-scale 2-d arrays,” *IEEE transactions on ultrasonics, ferroelectrics, and frequency control*, vol. 63, no. 6, pp. 803–816, 2016.
- [52] C. Anderson-Cook, “Statistical tools for nonlinear regression: a practical guide with s-plus and r examples:statistical tools for nonlinear regression: A practical guide with s-plus and r examples,” *Journal of The American Statistical Association - J AMER STATIST ASSN*, vol. 99, pp. 902–903, 09 2004.

Supplementary Data

		BF-data									
		super-resolution in x					super-resolution in z				
Intensity (dB)		1	10	20	30	40	1	10	20	30	40
$\sigma_{noise} = 0$ dB	$z = 5$ mm	2	17	$9 \cdot 10^3$	$8 \cdot 10^6$	$5 \cdot 10^{10}$	2	12	$7 \cdot 10^3$	$6 \cdot 10^6$	$3 \cdot 10^{10}$
	$z = 10$ mm	2	17	$10 \cdot 10^3$	$8 \cdot 10^6$	$5 \cdot 10^{10}$	2	13	$7 \cdot 10^3$	$6 \cdot 10^6$	$4 \cdot 10^{10}$
	$z = 15$ mm	2	16	$9 \cdot 10^3$	$7 \cdot 10^6$	$4 \cdot 10^{10}$	2	15	$8 \cdot 10^3$	$7 \cdot 10^6$	$4 \cdot 10^{10}$
	$z = 20$ mm	2	14	$8 \cdot 10^3$	$7 \cdot 10^6$	$4 \cdot 10^{10}$	2	17	$9 \cdot 10^3$	$8 \cdot 10^6$	$5 \cdot 10^{10}$
$\sigma_{noise} = 10$ dB	$z = 5$ mm	1	2	56	$5 \cdot 10^3$	$3 \cdot 10^6$	0	2	40	$3 \cdot 10^3$	$2 \cdot 10^6$
	$z = 10$ mm	1	2	56	$5 \cdot 10^3$	$3 \cdot 10^6$	1	2	42	$3 \cdot 10^3$	$2 \cdot 10^6$
	$z = 15$ mm	1	2	51	$4 \cdot 10^3$	$3 \cdot 10^6$	1	2	48	$4 \cdot 10^3$	$2 \cdot 10^6$
	$z = 20$ mm	1	2	47	$4 \cdot 10^3$	$2 \cdot 10^6$	1	2	55	$5 \cdot 10^3$	$3 \cdot 10^6$
$\sigma_{noise} = 20$ dB	$z = 5$ mm	0	1	4	34	$2 \cdot 10^3$	0	0	3	24	$1 \cdot 10^3$
	$z = 10$ mm	0	1	4	34	$2 \cdot 10^3$	0	0	3	25	$1 \cdot 10^3$
	$z = 15$ mm	0	1	3	31	$2 \cdot 10^3$	0	1	3	29	$2 \cdot 10^3$
	$z = 20$ mm	0	0	3	28	$2 \cdot 10^3$	0	1	3	33	$2 \cdot 10^3$
$\sigma_{noise} = 30$ dB	$z = 5$ mm	0	0	1	3	21	0	0	1	2	15
	$z = 10$ mm	0	0	1	3	21	0	0	1	2	16
	$z = 15$ mm	0	0	1	3	20	0	0	1	2	18
	$z = 20$ mm	0	0	1	2	18	0	0	1	3	21

Table 6.1: The super-resolution in both x - and z -direction for the beamformed images. The intensity and noise are given in dB and the depth of the scatterer z in mm.

		RF-data									
		super-resolution in x					super-resolution in z				
Intensity (V)		1	10	20	30	40	1	10	20	30	40
$\sigma_{noise} = 1$ V	$z = 5$ mm	1	41	$240 \cdot 10^3$	$2 \cdot 10^8$	$3 \cdot 10^{11}$	0	26	$149 \cdot 10^3$	$1 \cdot 10^8$	$2 \cdot 10^{11}$
	$z = 10$ mm	0	15	$89 \cdot 10^3$	$8 \cdot 10^8$	$1 \cdot 10^{11}$	0	4	$25 \cdot 10^3$	$2 \cdot 10^7$	$3 \cdot 10^{10}$
	$z = 15$ mm	0	8	$44 \cdot 10^3$	$4 \cdot 10^7$	$5 \cdot 10^{10}$	0	2	$9 \cdot 10^3$	$8 \cdot 10^6$	$1 \cdot 10^{10}$
	$z = 20$ mm	0	5	$26 \cdot 10^3$	$2 \cdot 10^8$	$3 \cdot 10^{10}$	0	0	$1 \cdot 10^3$	$1 \cdot 10^6$	$2 \cdot 10^9$
$\sigma_{noise} = 3$ V	$z = 5$ mm	0	3	650	$5 \cdot 10^4$	$8 \cdot 10^6$	0	2	400	$3 \cdot 10^4$	$5 \cdot 10^6$
	$z = 10$ mm	0	1	240	$2 \cdot 10^4$	$3 \cdot 10^6$	0	0	68	$6 \cdot 10^3$	$8 \cdot 10^5$
	$z = 15$ mm	0	1	120	$1 \cdot 10^4$	$1 \cdot 10^6$	0	0	24	$2 \cdot 10^3$	$3 \cdot 10^5$
	$z = 20$ mm	0	0	71	$6 \cdot 10^3$	$9 \cdot 10^5$	0	0	3	$3 \cdot 10^2$	$4 \cdot 10^4$
$\sigma_{noise} = 10$ V	$z = 5$ mm	0	1	6	47	668	0	0	3	29	417
	$z = 10$ mm	0	0	2	17	248	0	0	1	5	70
	$z = 15$ mm	0	0	1	9	122	0	0	0	2	25
	$z = 20$ mm	0	0	1	5	73	0	0	0	0	4
$\sigma_{noise} = 30$ V	$z = 5$ mm	0	0	0	1	2	0	0	0	1	1
	$z = 10$ mm	0	0	0	0	1	0	0	0	0	0
	$z = 15$ mm	0	0	0	0	0	0	0	0	0	0
	$z = 20$ mm	0	0	0	0	0	0	0	0	0	0

Table 6.2: The super-resolution in both x - and z -direction for the radiofrequency data. The intensity and noise are given in voltages and the depth of the scatterer z in mm.

Appendix

A.1 Optical beamforming

The procedure of imaging with FPALM consists of two steps: the activation and the readout/photobleaching, which can be seen in Figure A.1. The two steps are repeated until enough information for the desired image is obtained, or until all molecules have been photobleached. [12]

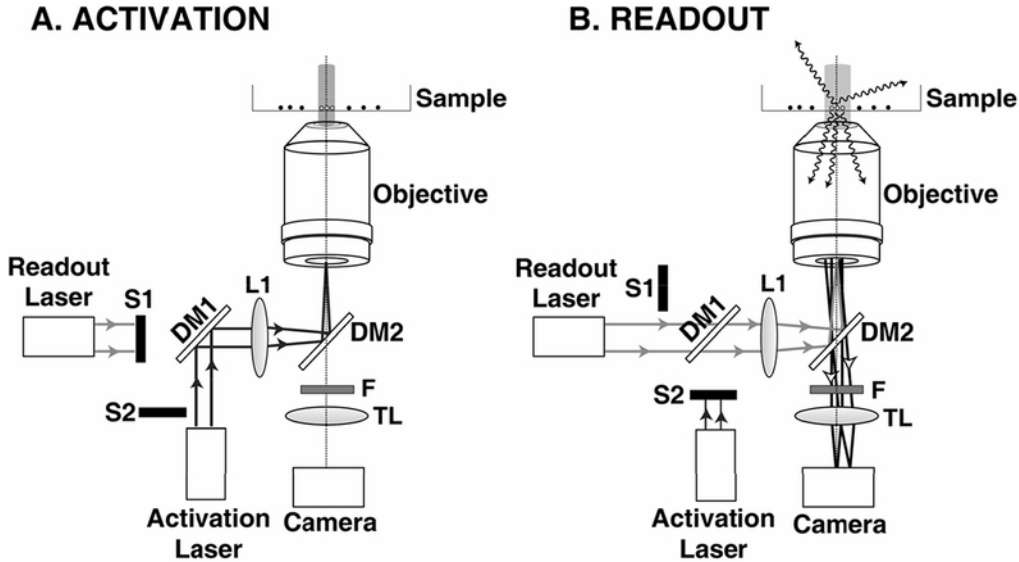


Figure A.1: A schematic representation of the optical beamforming in FPALM. [12]

1) Activation of the fluorophores

During the first step, mirror DM1 reflects the activation laser into lens L1, after which a second mirror DM2 makes sure that this laser ends up into the objective back aperture. [12] A shutter S1 blocks the readout laser during this activation phase.

2) Readout and photobleaching

During readout, shutter S1 is removed, while second shutter S2 blocks the activation laser. Now it is the readout beam which goes through mirror DM1, followed by lens L1 and mirror DM2 to be focused onto the objective back aperture. After this, the readout beam illuminates the sample in circular area (which approximates a Gaussian profile) to activate molecules to fluoresce. The objective collects the emitted fluorescence photons, after which the signal

is filtered to remove laser and scattered light, denoted with F. Now the signal, focused by the microscope tube lens TL, hits a camera and an image can be made. [12] Due to the photobleaching as described in 2.2.1, the number of visible molecules will decrease over time.

A.2 Ultrasound Beam Forming

Ultrasound sensors are able to both receive and transmit ultrasound signals. [17] When a sensor is hit by a signal with a specific phase, amplitude and waveform, the sensor can be excited. In this paragraph, two different ways of beamforming are discussed, respectively Linear Array Beam Forming and Phase Array Beam Forming.

- **Linear Array Beam Forming**

In Linear Array Beam Forming, the sensors in the array are divided into different sub-apertures, as can be seen in the left part of Figure A.2. Within each sub-group, the same waveform is transmitted, but with a different amplitude and different phase. [17] By shifting the sub-aperture over the array, many signals (the so called A-scan) can be obtained. With this A-scan, one can determine the structures in front of the sub-aperture over depth. Linear Array Beamformers are using information about the wave direction and the location of the sensor to combine the A-scans, with a fixed set of time-delays and weightings. The linear beams can not be steered, so they can image only the area in front of the aperture. However, when distributing the linear array sensors along a curve, one can obtain a larger field of view. [46], [47]

When applying focusing, one can generate higher pressures and thus higher spatial resolution, higher SNR and higher penetration depth. However, this also results in smaller beams, making it necessary to have more beams to cover the total field of view (FOV). Besides, the need for more transmission events will cause a decrease in frame rate. [17]

- **Phase Array Beam Forming**

Another way for image forming is Phase Array Beam Forming. This method is equal to that of Linear Array Beam Forming, but now each transmission is using the entire array aperture (see the right part of Figure A.2). This method is only possible if the pitch (the distance between the centres) is smaller than half of the wavelength. Otherwise, grating lobes will degrade the image quality. Since the beam can be controlled in direction, it can image a larger area compared to linear arrays. [17]

A.3 Find the point spread function

A.3.1 Determine the sound pressure

For now, a simple situation of a 1D-array with N transducer elements is considered, as shown in Figure A.3. From this figure, it becomes clear that the steering vector \vec{r} with length r can be rewritten as follows:

$$\vec{r} = r \left(\sin \theta, \sin \varphi, \sqrt{\cos^2 \theta - \sin^2 \varphi} \right) \quad (\text{A.1})$$

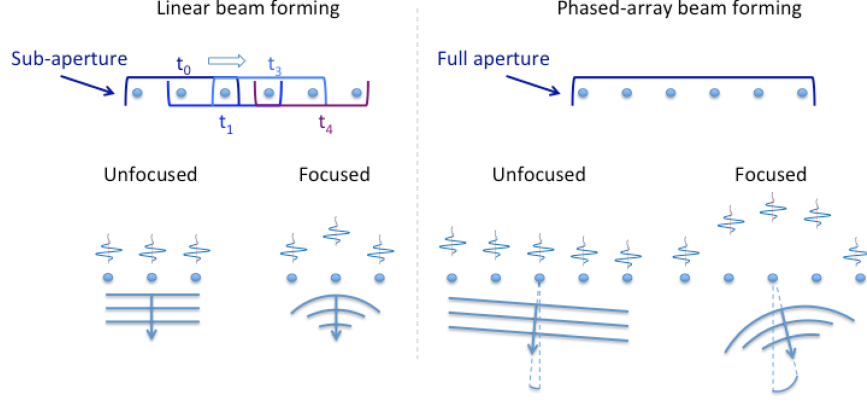


Figure A.2: Linear Array Beam Forming and Phased Array Beam Forming. [17]

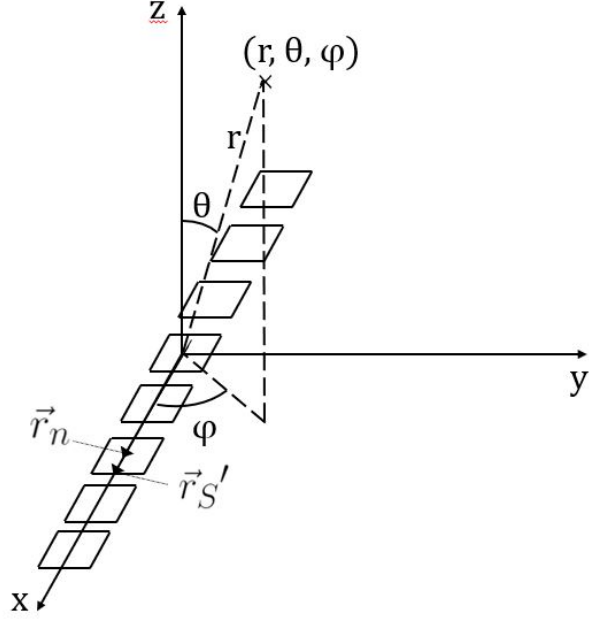


Figure A.3: The 1D-array and the sound field described in coordinates.

The velocity profiles on the surfaces are assumed to be the same: $v_0(t)$. Each transducer element, denoted by n , produces a sound pressure. At a certain point P , this pressure $p_n(\vec{r}, t)$ can be expressed as an Rayleigh integral over the n -th element surface S_n : [31]

$$p_n(\vec{r}, t) = \rho \frac{\partial v_0(t)}{\partial t} * \iint_{S_n} \frac{\delta\left(t - \frac{|\vec{r} - \vec{r}_n - \vec{r}'_S|}{c}\right)}{2\pi |\vec{r} - \vec{r}_n - \vec{r}'_S|} dS \quad (\text{A.2})$$

in which ρ represents the medium density and c the sound velocity in the medium. \vec{r} denotes the spatial vector of point P , \vec{r}_n equals the vector of the center of the n -th transducer element and \vec{r}'_S represents the relative vector of a source point on the surface of the n -th element compared to its center (see Figure A.3). The delta-function represents the impulse response of a single vibration. [31]

According the Rayleigh integral, spherical waves are emitted from each point in the plane $z = 0$,

all contributing to the total field in a point (x, y, z) . [6] This method is restricted to planar transducers. Therefore, the derived solution in this research only holds for these type of transducers. [48]

Combining the distribution of all different transducer elements N_T with weighting coefficients A_n in point P to reduce artifacts, results in the following transmitted sound pressure, in which $h_T(\vec{r}, t)$ represents the spatial impulse response of the transmitting array: [49]

$$\begin{aligned} p_T(\vec{r}, t) &= \rho \frac{\partial v_0(t)}{\partial t} * \sum_{n=1}^{N_T} A_n \iint_{S_n} \frac{\delta\left(t - \frac{|\vec{r} - \vec{r}_n - \vec{r}'_{S'}|}{c}\right)}{|\vec{r} - \vec{r}_n - \vec{r}'_{S'}|} dS \\ &= \rho \frac{\partial v_0(t)}{\partial t} * h_T(\vec{r}, t) \end{aligned} \quad (\text{A.3})$$

To describe the ultrasound pulse-echo process, the scattered pressure due to the m -th element, can be determined by the following equation: [50]

$$\begin{aligned} p_R(\vec{r}, \vec{r}_m, t) &= s(t) * \iint_{S_m} \frac{p_T\left(\vec{r}, t - \frac{|\vec{r}_R - \vec{r}'|}{c}\right)}{4\pi |\vec{r}_R - \vec{r}'|} dS \\ &= s(t) * p_T(\vec{r}, t) * \iint_{S_m} \frac{\delta\left(t - \frac{|\vec{r} - \vec{r}_m - \vec{r}'_{S'}|}{c}\right)}{|\vec{r} - \vec{r}_m - \vec{r}'_{S'}|} dS \end{aligned} \quad (\text{A.4})$$

in which again S_m and \vec{r}_m respectively represent the surface and the center vector of the m -th element, $\vec{r}'_{S'}$ equals the relative vector of the receiving point on the m -th element compared to its center and $s(t)$ denotes the scattering impulse response.

A.3.2 Find the ultrasound pulse-echo

Above equations can be used to express the received output voltage V_{out} , defined as the pressure wave at a certain point P due to a rigid small scatterer (diameter $\ll \lambda$). After scattering, the wave propagates through the medium and hits the element again. This impulse response of a receiving element is denoted with $g_R(t)$. The output voltage can be found by taking the convolution of this $g_R(t)$ with the obtained scattered pressure $p_R(\vec{r}, t)$. The total voltage can now be found by a superposition of all single voltages [51]:

$$\begin{aligned} V_{out}(\vec{r}, t) &= \sum_{m=1}^{N_R} g_R(t) * p_R(\vec{r}, \vec{r}_m, t) \\ &= g_R(t) * s(t) * p_T(\vec{r}, t) * h_R(\vec{r}, t) \end{aligned} \quad (\text{A.5})$$

Here, the spatial impulse response of the received array $h_R(\vec{r}, t)$ is introduced, which equals:

$$h_R(\vec{r}, t) = \sum_{m=1}^{N_R} \iint_{S_n} \frac{A_m \delta\left(t - \frac{|\vec{r} - \vec{r}_m - \vec{r}'_{S'}|}{c}\right)}{|\vec{r} - \vec{r}_m - \vec{r}'_{S'}|} dS \quad (\text{A.6})$$

in which A_m represents the weighting coefficient of the m -th element. [31] This apodization with A_m reduces the artefacts.

The velocity $v_0(t)$ at the surfaces of the elements can be found by taking the convolution of the

impulse response of the transmitting elements $g_T(t)$ with the input excitation $V_{in}(t)$: $v_0(t) = g_T(t) * V_{in}(t)$. Combining all equations, the scatterer at $(0, 0, |\vec{r}|)$ gives the following output voltage: [31]

$$V_{out}(\vec{r}, t) = \rho \left[g_R(t) * s(t) * \frac{\partial}{\partial t} (g_T(t) * V_{in}(t)) \right] * h_T(\vec{r}, t) * h_R(\vec{r}, t) \quad (\text{A.7})$$

The terms between the square brackets represent the simulated pulse, the responses of transducers and the backscattering included, and also the transmitted waveform. The array performance can be evaluated with the adoption of the PSF. In this case, the backscattering process is assumed to be frequency independent, and thus considered as scattering impulse response: $s(t) = \delta(t)$. [31]

A.3.3 Simplifications

For simplicity in calculation, the excitation pulse for the calculation of the PSF is assumed to be a wideband Gaussian waveform, which covers the whole bandwidth of the array. This pulse depends on the amplitude g_0 , the central frequency f_0 and the bandwidth Δf and is given by the following equation: [51]

$$pulse(t) = \begin{cases} g_0 \exp \left[-\frac{\pi^2 \Delta f^2 (t-t_0)^2}{\beta} \right] \sin(2\pi f_0 t) & t \geq 0 \\ 0 & \text{elsewhere} \end{cases} \quad (\text{A.8})$$

The output voltage is oscillating. By taking the maximum value of this voltage, one can obtain the maximum intensity. Therefore, the PSF can be determined by taking the maximum value of the output voltage in time: $PSF(\vec{r}) = \max(|V_{out}(\vec{r}, t)|)$, which can be considered as a spatial impulse response of the array. [31]

To speed up the computation of the PSF, one can use a narrowband assumption under the far-field approximation. To simplify the expressions, introduce $u = \sin \theta$, with θ as defined in Figure A.3. Then, the narrowband directivity A for a 1D array, is given as: [31]

$$A(u) = \text{sinc} \left(\frac{a}{\lambda} u \right) \quad (\text{A.9})$$

in which a represents the element dimension and λ the wavelength. [31]

Using again $u = \sin \theta$, one can simplify the expressions for $h_T^P(\vec{r}, t)$ and $h_R^P(\vec{r}, t)$. This results in the following expression for the output voltage V_{out} :

$$V_{out} = A^2(u) \cdot \{pulse(t) * h_T^P(u, t) * h_R^P(u, t)\} \quad (\text{A.10})$$

The time-domain version of the PSF is then given by the following: [31]

$$\begin{aligned} PSF(u, t) &= \max \left| \text{sinc}^2 \left(\frac{a}{\lambda} u \right) \{pulse(t) * h_T^P(u, t) * h_R^P(u, t)\} \right| \\ h_T^P(u, t) &= \sum_{n=1}^{N_T} \frac{A_n \delta \left(t - \frac{r_0}{c} - \frac{x_n u}{c} \right)}{r_0} \\ h_R^P(u, t) &= \sum_{m=1}^{N_R} \frac{A_m \delta \left(t - \frac{r_0}{c} - \frac{x_m u}{c} \right)}{r_0} \end{aligned} \quad (\text{A.11})$$

in which the n -th element is located at $(x_n, 0, 0)$ and the m -th element at $(x_m, 0, 0)$. The pulse is defined in equation (A.8). Looking at the above equations, one can see that the PSF is not dependent on the ϕ from figure A.3.

A.4 Localization Precision in RF-data with noise fluctuations

In the main text, the point spread function to determine the CRLB for RF-data is given. In this section, the maximal achievable resolution in this frequency domain in case of noise fluctuations will be given.

Considering noise fluctuations in the arrival time of the echoes (equation (2.3)), the resolution can then be determined in two steps: [9]

1) Determine the time precision

The time precision of the signal can be determined by estimating the error of the echo's arrival time at its maximum pressure. One way to find the standard deviation σ_τ is by using the Cramér-Rao Lower Bound, which will be thoroughly discussed in section 2.5. A second way to determine σ_τ is by directly measuring the standard deviation from experimental data. This second method is favorable, since it immediately takes into account all the sampling errors. [9] The time interval between two consecutive images is called the temporal resolution. [17] This is the resolution in frequency domain.

2) Determine the spatial precision

The resulting time precision from step 1) can be transformed into spatial precision by fitting a hyperboloid to the data. Since the time-of-flight model is not polynomial, one cannot determine the accuracy of the results directly from the timing error. [9] Instead, an asymptotic model is made to determine the back-propagation from the fitting to the resulting coordinates. [52] This back-propagation can be described by minimizing the sum of the residuals squared [9]:

$$S(x_0, y_0, z_0) = \sum_{i=1}^N (\tau_i - \hat{\tau}_i)^2 \quad (\text{A.12})$$

In equation (A.12), N represents the total number of transducers, τ_i the reception time as described in equation (2.3) and $\hat{\tau}_i$ the measured time of reception of the maximum echo. Using this method, combined with the variance-covariance matrix, one can estimate the position of the source: $(\hat{x}_0, \hat{y}_0, \hat{z}_0)$. [9] The squared deviation can be found in the diagonal elements of the covariance matrix. Using the Taylor expansion for the far-field approximation, one can find the following spatial variances [9]:

$$\begin{aligned} \text{Var}(\hat{x}_0) &\approx 12 \cdot \frac{(c \cdot \sigma_\tau)^2 \cdot z_0^2}{n \cdot L_x^2} \\ \text{Var}(\hat{y}_0) &\approx 12 \cdot \frac{(c \cdot \sigma_\tau)^2 \cdot z_0^2}{n \cdot L_y^2} \\ \text{Var}(\hat{z}_0) &\approx \frac{(c \cdot \sigma_\tau)^2}{4 \cdot n} \end{aligned} \quad (\text{A.13})$$

in which L_x and L_y are the apertures in respectively x - and y -direction, c equals the speed of sound, σ_t is the localisation precision of the peak and n represents the number of transducers in the aperture. [9] From the variances given in equation (A.13), the standard deviation for the position of the microbubble can easily be determined by taking the square root of the

variances: [23]

$$\begin{aligned}\sigma_{\hat{x}_0} &\approx 2\sqrt{3} \cdot \frac{c \cdot \sigma_\tau \cdot z_0}{\sqrt{n} \cdot L_x} \\ \sigma_{\hat{y}_0} &\approx 2\sqrt{3} \cdot \frac{c \cdot \sigma_\tau \cdot z_0}{\sqrt{n} \cdot L_y} \\ \sigma_{\hat{z}_0} &\approx \frac{c \cdot \sigma_\tau}{2 \cdot \sqrt{n}}\end{aligned}\tag{A.14}$$

It is important to realize that the above equations are in the frequency domain. This is, as stated before, the resolution for the radiofrequency data and describes the smallest spatial distance at which two different scatterers are distinguishable in the resulting image. [17]

Matlab Scripts

In this part, the used scripts to determine the localization precision are given, starting with the script for the RF-data, followed by the script for the BF-data.

B.1 RF-data

```
1 %% Make a clear workspace
2 clear all
3 clc
4 close all
5
6 %% Load all data
7 load('RF_002.mat')
8 load('MediaCoordinates_002.mat')
9 load('MatIn_002.mat')
10 rf_data1 = cell2mat(RFDataP);
11 img_data1 = cell2mat(ImgDataP);
12
13 %% Introduce constants and variables
14
15 pixelsize_x = 39.424e-6;    % pixelsize in x-direction in m
16 pixelsize_z = 24.64e-6;    % pixelsize in z-direction in m
17
18 c = 1540;                  % speed of sound in m/s
19 f = 15.625e6;              % frequency in Hz
20 lambda = c/f;              % wavelength in m
21
22 sigma_noise = db2mag(30);  % readout noise of the detector
23
24 %% Determine the positions of maximum intensity
25 max_x1 = []; max_z1 = []; coord_x0 = []; coord_z0 = [];
26
27 for i = 1:length(img_data1(1,1,1,:))           % for-loop
    to look at every timeframe
28     img_norm = img_data1(:,:, :, i);          % select
        certain image
```

```

29     [maxvalue , index] = max(img_norm(:));           % find
        position and value of max intensity
30     [max_z1(i), max_x1(i)] = ind2sub(size(img_norm), index); % save the
        positions of max intensity in x and z
31 end
32
33 img_x0_unit = pixelsize_x*max_x1;           % x-position according ImgData
        in meter
34 img_z0_unit = pixelsize_z*max_z1;           % z-position according ImgData
        in meter
35
36 for i = 1:length(MediaCoordinates)           % store the coordinates of the
        scatterer in x and z
37     coord = MediaCoordinates{i};
38     coord_x0(i) = coord(1); coord_z0(i) = coord(3);
39 end
40
41 coord_x0_unit = coord_x0;           % x-position according MediaCoordinates
        in meter
42 coord_z0_unit = coord_z0;           % z-position according MediaCoordinates
        in meter
43
44 %% Fit the parabolas to the RF-data
45
46 t = linspace(1,6144,6144);           % create a time-array
47 t_unit = t/(4*f);                     % convert to seconds
48 s = linspace(1,128,128);             % create a space-array
49 s_unit = s*lambda;                   % convert to meter
50 x_tau = linspace(1,128,128);         % create an array for the fit
51
52 points = []; tau_para = [];
53 max_array = []; max_tau = [];
54
55 for j = 1:256                           % go through all time frames
56     for i = 1:128                         % determine a rough estimate for every
        transducer element
57         index = min(rf_data1(:,i, :, j));
58         points(i, j) = min(find(rf_data1(:,i, :, j)==index)); % select
        one point for each element
59     end
60     tau = points(:, j);                   % select the chosen
        points for timeframe j
61     min_tau = find(tau == min(tau));       % find the minimum
        value to prevent errors
62     if min_tau-50<1
63         p_tau = polyfit(x_tau(1:min_tau+50), ... % fit a parabola to
        the points
64             tau(1:min_tau+50)', 2);

```

```

65     elseif min_tau+50>1280
66         p_tau = polyfit(x_tau(min_tau-50:1280) ,...
67             tau(min_tau-50:1280) ',2);
68     else
69         p_tau = polyfit(x_tau(min_tau-50:min_tau+50), ...
70             tau(min_tau-50:min_tau+50) ',2);
71     end
72     tau_para(:,j) = polyval(p_tau,x_tau);           % store
73     % the paraboles in an array
74     max_array(j) = find(tau_para(:,j)==min(tau_para(:,j))); % store
75     % the x-position of its maximum
76     max_tau(j) = min(tau_para(:,j));              % store
77     % the z-position of its maximum
78 end
79 tau_para_unit = tau_para/(4*f);                 % convert to seconds
80 max_array_unit = max_array*lambda;              % convert from pixels to
81 % meters
82 max_tau_unit = max_tau/(4*f);                   % convert the z-position of the
83 % maximum to seconds
84 rf_x0 = max_array;
85 rf_z0 = max_tau_unit*c/2 /pixelsize_z;
86 rf_x0_unit = max_array_unit;                    % x-position of the scatterer
87 % according the rf-data
88 rf_z0_unit = max_tau_unit*c/2;                 % z-position of the scatterer
89 % according the rf-data
90 %% Find the Fisher Information Matrix
91 voltage = linspace(1,40,10);                   % create an array of intensities
92 timeframe = 2;                                  % choose a certain time frame
93 N = 0;                                           % select number of frames on both sides
94 % of the chosen frame
95 I_11 = 0; I_12 = 0; I_13 = 0; I_14 = 0;        % create fisher-matrix
96 % components
97 I_21 = 0; I_22 = 0; I_23 = 0; I_24 = 0;
98 I_31 = 0; I_32 = 0; I_33 = 0; I_34 = 0;
99 I_41 = 0; I_42 = 0; I_43 = 0; I_44 = 0;
100 crlb_x=[]; crlb_z = [];                         % create arrays to save the
101 % crlb
102 % run for different intensities
103 for int=1:length(voltage)
104     display(['This is Iteration Number ', num2str(int)])
105     I = (voltage(int));

```

```

103
104 % run for different timeframes
105 for t = timeframe-N:timeframe+N
106     max_x = rf_x0(t);
107
108     % load and normalize the rf-approximation
109     para_norm = tau_para(:,t)/max(tau_para(:,t));
110     para_norm_prev = tau_para(:,t-1)/max(tau_para(:,t-1));
111
112     % determine the derivative in x- and z-direction
113     afgx_para = gradient(para_norm);
114     afgz_para = (para_norm-para_norm_prev)/(rf_z0(t)-rf_z0(t-1));
115
116     % fill up the fisher information matrix with the summation
117     I_11 = I_11 + (sum(afgx_para(1:max_x)))^2;
118     I_12 = I_12 + sum(afgx_para(1:max_x).*afgz_para(1:max_x));
119     I_13 = I_13 + sum(afgx_para(1:max_x).*para_norm(1:max_x));
120     I_14 = I_14 + sum(afgz_para(1:max_x));
121     I_22 = I_22 + (sum(afgz_para(1:max_x)))^2;
122     I_23 = I_23 + sum(para_norm(1:max_x).*afgz_para(1:max_x));
123     I_24 = I_24 + sum(afgz_para(1:max_x));
124     I_33 = I_33 + (sum(para_norm(1:max_x)))^2;
125     I_34 = I_34 + sum(para_norm(1:max_x));
126     I_44 = I_44 + 1;
127 end
128
129 % finish the components after the summation
130 I_11 = I_11 * (I/sigma_noise)^2; I_12 = I_12 * (I/sigma_noise)^2;
131 I_13 = I_13 * -I/(sigma_noise^2); I_14 = I_14 * -I/(sigma_noise^2);
132 I_21 = I_12; I_22 = I_22 * (I/sigma_noise)^2;
133 I_23 = I_23 * -I/(sigma_noise^2); I_24 = I_24 * -I/(sigma_noise^2);
134 I_31 = I_13; I_32 = I_23;
135 I_33 = I_33 * 1/(sigma_noise^2); I_34 = I_34 * 1/(sigma_noise^2);
136 I_41 = I_14; I_42 = I_24;
137 I_43 = I_34; I_44 = I_44 * 1/(sigma_noise^2);
138
139 % build the fisher information matrix
140 fish_para = [I_11 I_12 I_13 I_14;
141             I_21 I_22 I_23 I_24;
142             I_31 I_32 I_33 I_34;
143             I_41 I_42 I_43 I_44];
144
145 % determine the crlb in x- and z-direction in meter
146 crlb_para = fish_para.^(-1);
147 crlb_x_pixel(int) = crlb_para(1,1);
148 crlb_z_pixel(int) = crlb_para(2,2);
149 end
150

```

```

151 sigma_x = sqrt(crlb_x_pixel)*pixelsize_x; % convert from variance in
      pixels to standard deviation in meters
152 sigma_z = sqrt(crlb_z_pixel)*pixelsize_z; % convert from variance in
      pixels to standard deviation in meters
153
154 %% Save the results in recognizable names for later use
155 rf_s30_t2_crlbx = crlb_x;
156 rf_s30_t2_crlbz = crlb_z;
157 rf_s30_t2_sigmax = sigma_x;
158 rf_s30_t2_sigmaz = sigma_z;
159 rf_s30_t2_voltage = voltage;
160
161 %% Plot the crlb's
162 figure()
163 semilogy(voltage, sigma_x*1e6, '-o', 'DisplayName', '\sigma_x')
164 hold on; legend
165 semilogy(voltage, sigma_z*1e6, '-o', 'DisplayName', '\sigma_z')
166 xlabel('Voltage (V)'); ylabel('\sigma (\mu m)')
167 title('Maximum Likelihood'); grid on
168
169 %% Image the rf-data with parabolas
170 close all
171 for i = [50 100 150 200]
172     figure()
173     imagesc(s_unit*1000,t_unit*1e6,rf_data1(:,:,i))
174     imagesc(s_unit*1000,t_unit*1e6,[])
175     ylim([max_tau_unit(i)*1e6-0.2 max_tau_unit(i)*1e6+1]); hold on
176     title(['RF-data with time-of-flight-fitting for the scatterer at z
      = ', ...
177           mat2str(round(rf_z0_unit(i)*1000)), ' mm'])
178     xlabel('transducer array (mm)'); ylabel('time (\mu s)')
179     plot(s_unit*1000,tau_para_unit(:,i)*1e6,'-k','linewidth',2)
180     xlim([1 12]); ylim([26.6 27.6])
181 end
182
183 %% Plot the parabolas in 1 figure
184 close all
185 tau_para_unit_norm = [];
186 for i = 1:length(tau_para_unit)
187     tau_para_unit_norm(:,i) = -tau_para_unit(:,i)/min(tau_para_unit(:,i)
      ));
188 end
189 tau_para_unit_norm = tau_para_unit_norm + ones(size(tau_para_unit_norm)
      )*2;
190
191 figure()
192 for i = [50 100 150 200]
193     plot(s_unit*1000,tau_para_unit(:,i)/max(tau_para_unit(:,i)), ...

```

```

194         'linewidth',2,'DisplayName',[ 'z = ',mat2str(round(rf_z0_unit(i)
           *1000)), ' mm']]
195     hold on
196 end
197 legend
198 xlabel('transducer array (mm)'); ylabel('tof/tof_{max}')
199 title('Time Of Flight for different depths')
200
201 %% Compare the scatterer positions according the RF-data, the ImgData
    and the Coordinates
202
203 % the x-range from MediaCoordinates goes from -A to A. To compare these
204 % coordinates with the other datasets, it is moved such that it only
    has
205 % positive values: from 0 to 2A.
206 coord_x0_unit_moved = coord_x0_unit + ones(size(coord_x0_unit))*length(
    coord_x0_unit)/2*pixelsize_x;
207
208 figure()
209 for i = round(linspace(1,256,10))
210     plot(rf_x0_unit(i)*1000,rf_z0_unit(i)*1000,'-or')
211     hold on
212     plot(coord_x0_unit_moved(round(i/2))*1000,coord_z0_unit(round(i/2)
        )*1000,'-*b')
213     plot(img_x0_unit(i)*1000,img_z0_unit(i)*1000,'-^k')
214 end
215 plot(rf_x0_unit*1000,rf_z0_unit*1000,'-r')
216 plot(coord_x0_unit_moved*1000,coord_z0_unit*1000,'-b')
217 plot(img_x0_unit*1000,img_z0_unit*1000,'-k')
218 hold on; legend('Time-Of-Flight from RF-data','MediaCoordinates','
    Maximum Intensity from BF-data'); grid on
219 xlabel('x (mm)'); ylabel('z (mm)')
220 title('Position of the scatterer according the different data')

```

B.2 BF-data

```
1 %% Make a clear workspace
2 clear all
3 clc
4 close all
5
6 tic
7 %% Load all data
8 load('RF_002.mat')
9 load('MediaCoordinates_002.mat')
10 load('MatIn_002.mat')
11 rf_data1 = cell2mat(RFDataP);
12 img_data1 = cell2mat(ImgDataP);
13
14 %% Introduce constants and variables
15
16 pixelsize_x = 39.424e-6;    % pixelsize in x-direction in m
17 pixelsize_z = 24.64e-6;    % pixelsize in z-direction in m
18
19 c = 1540;                  % speed of sound in m/s
20 f = 15.625e6;             % frequency in Hz
21 lambda = c/f;            % wavelength in m
22
23 sigma_noise = db2mag(30); % readout noise of the detector
24
25 %% Determine the positions of maximum intensity
26 img_x0 = []; img_z0 = []; coord_x0 = []; coord_z0 = [];
27
28 for i = 1:length(img_data1(1,1,1,:))           % for-loop
29     to look at every timeframe
30     img_norm = img_data1(:,:,i);               % select
31     [maxvalue,index] = max(img_norm(:));       % find
32     position and value of max intensity
33     [img_z0(i), img_x0(i)] = ind2sub(size(img_norm),index); % save the
34     positions of max intensity in x and z
35 end
36
37 img_x0_unit = pixelsize_x*img_x0;             % x-position according ImgData
38     in meter
39 img_z0_unit = pixelsize_z*img_z0;             % z-position according ImgData
40     in meter
41
42 for i = 1:length(MediaCoordinates)            % store the coordinates of the
43     scatterer in x and z
44     coord = MediaCoordinates{i};
```

```

39     coord_x0(i) = coord(1); coord_z0(i) = coord(3);
40 end
41
42 coord_x0_unit = coord_x0*lambda;           % x-position according
      MediaCoordinates in meter
43 coord_z0_unit = coord_z0*lambda;           % z-position according
      MediaCoordinates in meter
44
45 %% Find the Fisher Information Matrix with a Gaussian Fit
46
47 intensity = db2mag(linspace(1,40,10));      % create an array of
      intensities
48 timeframe = 50;                            % choose a certain time
      frame
49 N = 0;                                       % select number of frames
      on both sides of the chosen frame
50
51 I_11 = 0; I_12 = 0; I_13 = 0; I_14 = 0;      % create fisher-matrix
      components
52 I_21 = 0; I_22 = 0; I_23 = 0; I_24 = 0;
53 I_31 = 0; I_32 = 0; I_33 = 0; I_34 = 0;
54 I_41 = 0; I_42 = 0; I_43 = 0; I_44 = 0;
55 crlb_x=[]; crlb_z = [];                     % create arrays to save the
      crlb
56 xx = linspace(1,1024,1024);                 % create vectors for the
      gaussian fit
57 zz = linspace(1,325,325);
58
59 % run for different intensities
60 for int=1:length(intensity)
61     display(['This is Iteration Number ', num2str(int)])
62     I = intensity(int);
63
64     % run for different timeframes
65     for t = timeframe-N:timeframe+N
66
67         % Load the image
68         img_1 = img_data1(:, :, :, t);
69         max_x = img_x0(t);                   % find the x- position
            of the maximum intensity for the chosen scatterer
70         max_z = img_z0(t);                   % find the z- position
            of the maximum intensity for the chosen scatterer
71
72         % Define PSF
73         img_1_z = img_1(:, max_x);           % define the peak to
            approximate in x
74         img_1_x = img_1(max_z, :);           % define the peak to
            approximate in z

```

```

75
76     fx = fit (zz.',img_1_x.', 'gauss1');           % fit a Gaussian to the
           peak in x
77     psf_x = fx (zz);                             % save the psf in x
78     fz = fit (xx.',img_1_z, 'gauss1');           % fit a Gaussian to the
           peak in z
79     psf_z = fz (xx);                             % save the psf in z
80
81     psf_x_norm = psf_x/max(psf_x);               % normalize the psf
82     psf_store (:,t) = psf_x_norm;                % store the psf
83
84     afgx_gauss = gradient (psf_x_norm);          % compute the
           derivative in x
85     afgz_gauss = (psf_x_norm-psf_store (:,t-1))/(img_z0(t)-img_z0(t-1)); % compute the derivative in z
86
87     I_11 = I_11 + sum (afgx_gauss.^2);           % fill the fisher
           components
88     I_22 = I_22 + sum (afgz_gauss.^2);
89     I_33 = I_33 + sum (psf_x_norm.^2);
90     I_44 = I_44 + 1;
91 end
92
93 % finish the components after the summation
94 I_11 = I_11 * (I/sigma_noise)^2;
95 I_22 = I_22 * (I/sigma_noise)^2;
96 I_33 = I_33 * 1/(sigma_noise^2);
97 I_44 = I_44 * 1/(sigma_noise^2);
98
99 % build the fisher information matrix
100 fish_gauss = [I_11 I_12 I_13 I_14;
101               I_21 I_22 I_23 I_24;
102               I_31 I_32 I_33 I_34;
103               I_41 I_42 I_43 I_44];
104
105 % determine the crlb in x- and z-direction in meter
106 crlb_gauss = fish_gauss.^(-1);
107 crlb_x_pixel (int) = crlb_gauss (1,1);
108 crlb_z_pixel (int) = crlb_gauss (2,2);
109 end
110
111 sigma_x = sqrt (crlb_x_pixel)*pixelsize_x;      % convert from variance in
           pixels to standard deviation in meter
112 sigma_z = sqrt (crlb_z_pixel)*pixelsize_z;      % convert from variance in
           pixels to standard deviation in meter
113
114 %% Save the results in recognizable names for later use
115 bf_s30_t50_crlbx = crlb_x;

```

```

116 bf_s30_t50_crlbz = crlb_z;
117 bf_s30_t50_sigmax = sigma_x;
118 bf_s30_t50_sigmaz = sigma_z;
119 bf_s30_t50_intensity = intensity;
120
121 %% Plot the crlb's
122
123 figure()
124 semilogy(mag2db(intensity), sigma_x*1e6, '-o', 'DisplayName', '\sigma_x'
125 )
126 hold on; legend
127 semilogy(mag2db(intensity), sigma_z*1e6, '-o', 'DisplayName', '\sigma_z')
128 xlabel('Intensity (dB)'); ylabel('\sigma (\mu m)')
129 title('Maximum Likelihood'); grid on
130
131 %% Plot the Gaussian Approximation
132
133 close all
134 figure()
135 for i = [50 100 150 200]
136     plot(psf_store(:,i), 'DisplayName', num2str(i))
137     hold on
138 end
139 legend
140 xlim([150 170])

```